



Nonlinear dynamics of unstably stratified two-layer shear flow in a horizontal channel

A. Kalogirou^{1,†} and M.G. Blyth²

¹School of Mathematical Sciences, University of Nottingham, University Park, Nottingham NG7 2RD, UK

²School of Mathematics, University of East Anglia, Norwich Research Park, Norwich NR4 7TJ, UK

(Received 9 June 2022; revised 23 November 2022; accepted 11 December 2022)

The Rayleigh–Taylor instability at the interface of two sheared fluid layers in a horizontal channel is investigated in the absence of inertia. The dynamics of the flow is described by a nonlinear lubrication equation which is solved numerically for adverse density stratifications. The early-time dynamics features a number of finger-like protrusions of different heights at the interface. The fingers travel at different speeds leading to a sequence of merging events after which the interface eventually settles to a near-saturated state, comprising only one finger that includes most of the lower fluid. For sufficiently large density stratifications, the final state spans the height of the channel and includes two thin fluid films at each wall, both of which undergo chaotic dynamics, but finite-time touch-down/touch-up is shown to be precluded by the shear flow. An asymptotic analysis in the large-Bond-number limit (intense density stratification) reveals the finer structure of the final state including Landau–Levich-type connection regions. The asymptotic solutions are compared with numerical results of the lubrication model as well as direct numerical simulations, and excellent agreement is observed between the three in terms of interfacial structure, wave speed and film thicknesses.

Key words: channel flow, lubrication theory

1. Introduction

The Rayleigh–Taylor (RT) instability occurs at the interface between two superposed fluid layers when the overlying fluid is the more dense and it falls into the lower density fluid under the action of gravity. Given its many applications in nature and in technology (e.g. Sharp 1984; Kull 1991), the RT instability has been studied extensively both

† Email address for correspondence: Anna.Kalogirou@nottingham.ac.uk

experimentally (e.g. Lewis 1950; Emmons, Chang & Watson 1960; Cole & Tankin 1973; Fermigier *et al.* 1992) and theoretically (e.g. Rayleigh 1883; Taylor 1950; Chandrasekhar 1981; Yiantsios & Higgins 1989; Newhouse & Pozrikidis 1990), with the focus on the case of a thin viscous liquid resting on a horizontal surface or hanging on the underside of a plate. In the equilibrium configuration the interface between the two fluids is flat. A small-amplitude perturbation to this rest state undergoes linear growth followed by the formation of pendant drops (Yiantsios & Higgins 1989; Elgowainy & Ashgriz 1997) or mushroom-shaped structures (Newhouse & Pozrikidis 1990) in the nonlinear regime. In certain cases the RT instability can be completely suppressed by using an electric field (Taylor & McEwan 1965; Tseluiko & Papageorgiou 2007; Cimpeanu, Papageorgiou & Petropoulos 2014; Anderson *et al.* 2017), a temperature gradient (Kopbosynov & Pukhnachev 1986; Burgess *et al.* 2001) or an insoluble surfactant (Frenkel & Halpern 2017; Kalogirou 2018), or through vertical vibrations of the wall (Wolf 1970) or the introduction of wall curvature (Trinh *et al.* 2014). The presence of a shear flow can lead to a nonlinear saturation of the RT instability (Babchin *et al.* 1983; Frenkel & Halpern 2000; Halpern & Frenkel 2001), in which case the flow can be described by a Kuramoto–Sivashinsky equation (Hooper & Grimshaw 1985).

In this work we consider the RT instability that emerges at the interface between two immiscible viscous fluids in a horizontal channel which are undergoing shear flow due to the horizontal translation of the upper channel wall. Inertia is neglected so that instability due to viscosity stratification does not occur (Yih 1967). This system is susceptible to the early-stage linear growth alluded to above and a formal linear stability analysis demonstrates that small-amplitude wave-like disturbances are unstable if their wavenumber lies in a range that is subtended between zero and a finite cut-off value (assuming non-zero interfacial tension) (Chandrasekhar 1981). Thus the instability is essentially long-wave in character and with this in mind we focus our attention on long-wave perturbations. In particular we study the dynamics mainly via a nonlinear evolution equation that we derive and which includes the effects of surface tension, viscosity stratification and gravity, but ignores inertia.

Interestingly, even though related lubrication equations have been obtained by several other authors (Hammond 1983; Yiantsios & Higgins 1989; Oron, Davis & Bankoff 1997; Bertozzi & Pugh 1998; Jensen 2000; Lister *et al.* 2006; Tseluiko & Papageorgiou 2007), investigations of the validity of such equations through comparisons with experimental data or direct numerical simulations (DNS) have been limited. Anderson *et al.* (2017) obtained a non-local equation describing the evolution of an electrified viscous thin film wetting the underside of a wall, and carried out DNS to assess the accuracy of the asymptotic model. In this work we also perform DNS, and attempt qualitative comparisons to examine the validity of our numerical results based on the lubrication equation, even for parameter sets outside the applicability region of the model.

A key parameter in our problem is the Bond number, which acts as a measure of the relative strength of gravitational and surface tension forces. In our case adverse density stratification is in place for any positive value of the Bond number, leading to RT instability and the appearance of large-amplitude protrusions at the fluid–fluid interface. As we shall see, these protrusions initially take the form of individual fingers that travel in the same direction as the basic shear flow. The emergence of such fingers is of course common in RT phenomena; what is of particular interest here is the way in which these fingers are advected with the flow and interact with one another. In fact we see in our simulations that a coarsening of the dynamics occurs as the fingers run into one another, following a sequence of merging events that leads ultimately to the formation of a residual, solitary

finger which propagates with a very nearly fixed form and at a near-constant speed. When the Bond number is sufficiently large, this solitary wave spans the whole of the channel height and, in so doing, effectively (almost) segregates the two fluids. We also establish that the interface may not achieve touch-down or touch-up at the channel walls in finite time. We note that singularity formation has been investigated analytically in related thin-film flow studies (e.g. Bertozzi & Pugh 1998; Tseluiko & Papageorgiou 2007), where uniform boundedness of solutions has been rigorously established.

In § 2 we introduce the governing equations and present the lubrication model partial differential equation (the derivation is provided in an appendix). In § 3 we present and discuss the results of unsteady numerical simulations of the model equation (§ 3.1) to reveal the coarsening dynamics mentioned above and the eventual emergence of fixed-form travelling-wave solutions. The latter are investigated using a continuation method in § 3.3, and the results are compared with those obtained from DNS of the full Stokes equations in § 3.4. Further insight into the shape of the final travelling-wave state is attained in § 4 via a large-Bond-number asymptotic analysis that also reveals a simple leading-order formula for the wave speed which depends only on the viscosity stratification parameter. In § 5 we summarise our findings.

2. Mathematical model

We consider an unstably stratified two-fluid flow in a horizontal channel of fixed height d , with the top fluid (labelled as fluid 2) being heavier than the bottom fluid (labelled as fluid 1) such that the fluid densities satisfy $\rho_2 > \rho_1$. The two fluids have generally different viscosities $\mu_1 \neq \mu_2$, and the flow in the channel is driven by the horizontal motion of the upper channel wall with speed U . The problem is expressed in non-dimensional form by rescaling lengths with d , velocities with U , pressures with $\mu_1 U/d$ and time with d/U . We neglect fluid inertia and study the dynamics under the conditions of Stokes flow.

We define a Cartesian coordinate system, with x being the horizontal coordinate, y the vertical coordinate and t denoting time. In non-dimensional terms, the channel walls are at $y = 0$ and $y = 1$ and the fluids are separated by an interface at $y = h(x, t)$. Defining the velocity vector $\mathbf{u}_j = (u_j, v_j)$ in each fluid ($j = 1, 2$), where the velocity components are space- and time-dependent, the dynamics within each fluid layer is governed by the non-dimensional continuity and Stokes equations:

$$\nabla \cdot \mathbf{u}_j = 0, \quad 0 = -\nabla p_j + m_j \nabla^2 \mathbf{u}_j - \frac{r_j}{(r-1)} \frac{B}{C} \hat{\mathbf{y}}, \quad (2.1)$$

where $p_j = p_j(x, y, t)$ is the fluid pressure, $\nabla = (\partial_x, \partial_y)$ is the gradient operator and $\hat{\mathbf{y}} = (0, 1)^T$ is the unit vector that points in the opposite direction to the gravitational force. The parameters $m_1 = 1$, $m_2 = m$, $r_1 = 1$ and $r_2 = r$, where $m = \mu_2/\mu_1$ and $r = \rho_2/\rho_1$ are the viscosity ratio and the density ratio, respectively. The capillary number, C , and the Bond number, B , are defined by

$$C = \frac{\mu_1 U}{\gamma} > 0, \quad B = \frac{(\rho_2 - \rho_1)gd^2}{\gamma} = (r-1) \frac{\rho_1 gd^2}{\gamma} > 0, \quad (2.2a,b)$$

where γ is the interfacial tension and g is the acceleration due to gravity. The boundary conditions at the channel walls and at the interface are

$$\mathbf{u}_1 = (0, 0) \quad \text{at } y = 0; \quad \mathbf{u}_2 = (1, 0) \quad \text{at } y = 1; \quad (2.3a)$$

$$\mathbf{u}_1 = \mathbf{u}_2, \quad [(\mathbf{n} \cdot \boldsymbol{\sigma}_j) \cdot \mathbf{n}]_2^1 = C^{-1} \kappa, \quad [(\mathbf{n} \cdot \boldsymbol{\sigma}_j) \cdot \mathbf{t}]_2^1 = 0 \quad \text{at } y = h(x, t), \quad (2.3b)$$

where the jump notation $[f_j]_2^1 = f_1 - f_2$ is used. The last two equations in (2.3b) are the interfacial normal and tangential stress jumps, respectively, where σ_j is the (dimensionless) stress tensor in fluid j , defined by

$$\sigma_j = -p_j \mathbf{I} + (\nabla \mathbf{u} + (\nabla \mathbf{u})^T), \quad j = 1, 2, \tag{2.4}$$

and \mathbf{I} is the identity matrix. The unit normal vector \mathbf{n} at the interface (pointing into the lower fluid), the unit tangent vector \mathbf{t} at the interface and the interfacial curvature κ are given by

$$\mathbf{n} = \frac{(h_x, -1)}{(1 + h_x^2)^{1/2}}, \quad \mathbf{t} = \frac{(1, h_x)}{(1 + h_x^2)^{1/2}}, \quad \kappa = \frac{h_{xx}}{(1 + h_x^2)^{3/2}}. \tag{2.5a-c}$$

Following Ooms, Segal & Cheung (1985), we impose the constraint that the total flow rate through the channel,

$$Q(t) = \int_0^{h(x,t)} u_1(x, y, t) dy + \int_{h(x,t)}^1 u_2(x, y, t) dy, \tag{2.6}$$

is fixed at time t so that there is no pressure drop over a domain of specified length in the x direction.

The unstably stratified system is characterised by the appearance of long waves at the interface (Yiantsios & Higgins 1989). Consequently, exploiting the disparity between the x and y length scales, we perform a lubrication analysis to derive the following model system that will allow us to study the nonlinear spatio-temporal interfacial dynamics (see Appendix A for a detailed derivation):

$$h_t + q_x = 0, \quad \text{with } q = \mathcal{D}^{-1} \left(mh^2 H_1 + \frac{1}{3} h^3 (1 - h)^3 H_2 \mathcal{F} \right), \tag{2.7a,b}$$

where $\mathcal{D}, H_1, H_2, \mathcal{F}$ are all functions of h and are defined by

$$\mathcal{D}(h) = m^2 h^4 + 2mh(1 - h) \left(2 - h(1 - h) \right) + (1 - h)^4 > 0, \tag{2.8a}$$

$$H_1(h) = (m - 1)h^3 + (Q - 1)(m - 1)h^2 + (1 - 2Q)h + (3Q - 1), \tag{2.8b}$$

$$H_2(h) = (1 - h) + mh > 0, \tag{2.8c}$$

$$\mathcal{F}(h) = C^{-1} (Bh_x + h_{xxx}). \tag{2.8d}$$

The functions \mathcal{D} and H_2 are positive provided that $0 < h < 1$, while the functions H_1 and \mathcal{F} can each be of either sign depending on the values of $Q(t), h_x$ and h_{xxx} . The lubrication model presented above is similar to the model of Tilley, Davis & Bankoff (1994) and it reduces to those obtained in related studies on channel flows with surfactant (Blyth & Pozrikidis 2004; Frenkel & Halpern 2017; Kalogirou & Blyth 2020), in the case when surfactant is neglected.

Small-amplitude long-wave disturbances are unstable according to (2.7) as is expected in the presence of adverse density stratification, $B > 0$, when gravity has a destabilising effect (Oron *et al.* 1997). Of particular interest here is the character of the nonlinear wave development as the interfacial amplitude grows beyond the confines of the linear regime. To this end, in the next section we focus on carrying out numerical simulations of the evolution equation (2.7) in a domain that is sufficiently large, to capture the instability due to density stratification.

3. Numerical results

3.1. Time-dependent simulations of the lubrication equation (2.7)

The lubrication equation (2.7) is solved numerically using a pseudospectral scheme (e.g. Trefethen 2000) on a periodic domain $[-L, L]$ and the unconditionally stable Crank–Nicolson method is used for the time discretisation. The discretised nonlinear system is solved at each time level by using Newton’s method. The (unknown) flow rate $Q(t)$ is calculated at each time step by imposing the zero-pressure-drop condition (A12), which is done numerically by setting the integral of the pressure gradient (A11) to zero and solving for $Q(t)$ (integrals are approximated by the trapezoidal rule). In all the simulations presented in this work, the (half) domain length is fixed to $L = 28$, which is sufficiently large to capture the phenomena of interest. Typically, 512 grid points are used to discretise the spatial domain, so the grid resolution is $2L/512 = 0.0194$, and a time step of size 0.05 is found to be sufficient to produce accurate results.

The initial condition corresponds to a sinusoidal disturbance superimposed on a flat interface at uniform height h_0 , and is given by

$$h(x, 0) = h_0 \left[1 + h_A \cos \left(\frac{n\pi x}{L} \right) \right], \quad (3.1)$$

where h_A is a constant and n is an integer. In what follows we describe the dynamics for the particular case $h_A = 0.2$ and $n = 1$. Following extensive simulations with other choices of these parameters (some further comment on which is provided below), including combinations of Fourier modes and amplitudes h_A selected from a random distribution, this was found to be representative of the dynamics that is observed. Unless otherwise stated, the parameters used in the numerical computations are $h_0 = 0.2$, $m = 0.5$, $C = 10^{-3}$ and $B = 1$.

Interfacial profiles at different stages of the simulation starting from the initial condition (3.1) and using the aforementioned parameter set are shown in figure 1. At early times a number of protrusions, hereinafter referred to as fingers, appear on the interface. In this case six fingers emerge, as can be seen in figure 1(a–c) corresponding to $t = 15, 20, 35$. Intuition suggests that the number of fingers will be dependent on the size of the Bond number, since a greater density disparity between the two fluids should correspond to a greater susceptibility to interfacial instability. While in the present results it takes approximately 35 time units for all six fingers to clearly form at the interface, we note that for larger values of B more fingers develop and also these emerge earlier in the simulation.

The number of fingers formed can be estimated using the growth rates determined from linear theory (e.g. Tseluiko & Papageorgiou 2007). These are calculated from (2.7) by writing $h = h_0 + A \exp(iKx + \sigma t) + \text{c.c.}$ (complex conjugate), and linearising on the basis that $A/h_0 \ll 1$ with a view to calculating σ for a prescribed wavenumber K (more details are provided in Appendix B). In figure 2, the linear growth rate, $\text{Re}(\sigma)$, is plotted against the spatial frequency $k = LK/\pi$ for various values of the Bond number B . In the context of the numerical simulations of the evolution equation (2.7), the variable k is taken to be an integer corresponding to the number of wavelengths that fit exactly into the computational domain of length $2L$. The fastest growing mode in the numerical simulation corresponds to the spatial frequency closest to that which maximises the growth rate, namely $k_{\max} = (L/\pi)\sqrt{B/2}$ (see Appendix B). For example, when $L = 28$ we have $k_{\max} \approx 6$ for $B = 1$ and $k_{\max} \approx 9$ for $B = 2$, the former prediction being in line with the six fingers that are observed in figure 1(c). The cut-off wavenumber for linear instability is $K_c = \sqrt{B}$ so that the range of unstable wavenumbers depends solely on the Bond number (see also Oron

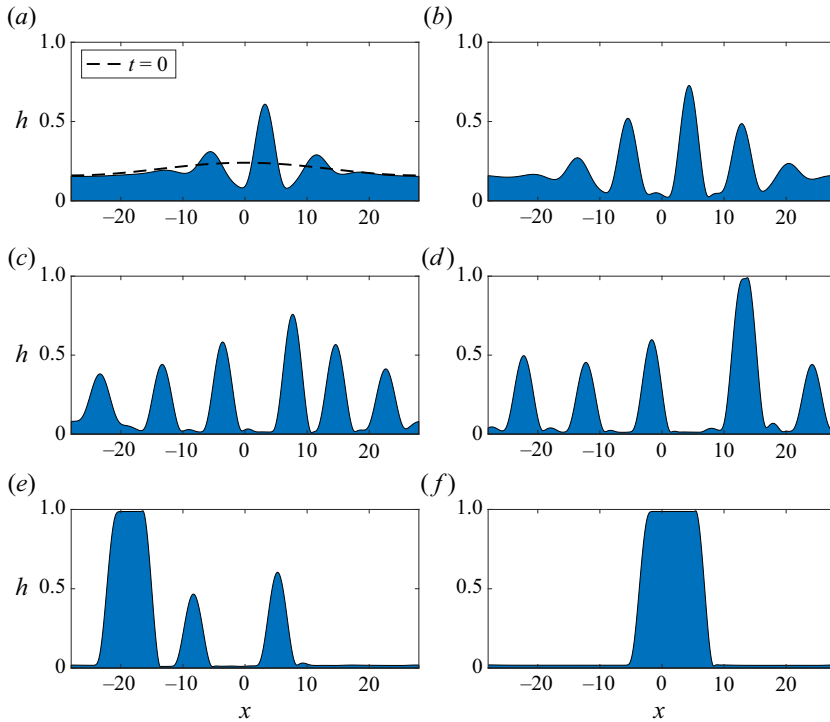


Figure 1. Interfacial profiles obtained at different times (a) $t = 15$, (b) $t = 20$, (c) $t = 35$, (d) $t = 50$, (e) $t = 100$ and (f) $t = 200$ for the parameter values $h_0 = 0.2$, $m = 0.5$, $C = 10^{-3}$ and $B = 1$. Starting from an initial condition of the form (3.1) with $h_A = 0.2$ and $n = 1$ (also shown with a broken line in panel a), six distinct fingers are seen to develop at early times in the simulation. These then get closer to the lower wall and slowly drift to the right due to background shear flow. The tallest finger travels faster and eventually merges with the finger directly in front of it. The merging dynamics continues to take place until a single wide finger remains that almost touches both channel walls. The solution seen in (f) has been shifted to the right by a distance $L = 28$ for better visualisation of the final finger. The time evolution of the interfacial profile can be seen in the supplementary movie available at <https://doi.org/10.1017/jfm.2022.1070>.

et al. 1997). Accordingly, in the simulations we must choose integer $k < LK_c/\pi$ in order to observe instability.

Finger formation similar to that seen in figure 1 has also been observed in a related study of channel flow by Mavromoustaki, Matar & Craster (2010). In the absence of the shear flow (so when the upper wall is stationary), the finger pattern in the interfacial profile retains the symmetry of the initial condition (3.1) approximately $x = 0$ (see related studies on static liquid film configurations, for example those by Yiantsios & Higgins (1989), Bertozzi & Pugh (1998), Tseluiko & Papageorgiou (2007), Wang, Mählmann & Papageorgiou (2009), Barannyk *et al.* (2015) and Wang & Papageorgiou (2018)). Here the symmetry is broken by the superimposed shear flow and consequently the interfacial profile tends to drift in the positive x direction. The individual fingers (as seen in the various panels of figure 1) travel more or less holding their shape, size and speed. Generally speaking, taller fingers have greater volume and move faster, as is confirmed in § 3.3. As a result the tallest finger eventually catches up with the finger directly in front of it, and the pair subsequently merge to form a larger finger whose volume is approximately the sum of the two individual volumes. An example can be seen in figure 1(c,d), where the interfacial profiles are displayed at $t = 35, 50$. After this first coalescence, the tallest

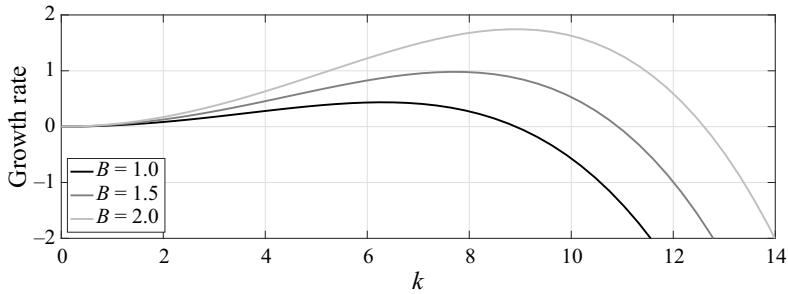


Figure 2. Linear growth rate for different values of the Bond number, plotted against $k = (L/\pi)K$, where K is the wavenumber and $L = 28$ is the (half) domain length. Parameter values for h_0, m, C are the same as in figure 1. A positive growth rate is supported for wavenumbers in the range $K \in (0, \sqrt{B})$, so interfacial instability is enhanced as the value of B increases. The maximum growth rate occurs at $k_{max} = (L/\pi)\sqrt{B/2}$.

finger has gained sufficient volume to approach the upper channel wall (see figure 1d). The merging process continues so that the number of fingers gradually diminishes until only a single, rather wide, finger remains (see figure 1f); this finger essentially combines the individual volumes of all fingers from the earlier stage of the simulation, with any deficit accounted for in the thin lower fluid film that comprises the remainder of the flow domain. Note that despite the apparently rather steep slope on either side of the finger, the scales are such that the gradient here is modest, so that the legitimacy of the assumed lubrication approximation ought to be maintained. With reference to alternative choices of initial condition mentioned above, broadly similar dynamics is observed, including the occurrence of merging events, the only difference being the number of final-state fingers (akin to that at $t = 200$ in figure 1) that are ultimately obtained. Similar coarsening dynamics has been reported by Glasner & Witelski (2003) and Kitavtsev (2014) who investigated dewetting of thin films, as well as by Chang, Demekhin & Kalaidin (2000) and Razis *et al.* (2014) in their studies of roll wave structures propagating down an inclined plane.

The merging events just described can also be seen in the evolution of the displacement norm $\|h - h_0\|_2$ shown in figure 3(a), where each of the sudden upward steps in the curve corresponds to the merging of a pair of fingers. The final merging event occurs at around $t = 150$ when the norm reaches the final plateau, and after this time the solitary finger propagates downstream essentially retaining the same form for the remainder of the simulation. Also shown in figure 3 is the trace of the interfacial minimum and maximum during the simulation. The minimum first decreases until around $t = 35$ when the interface almost makes contact with the bottom wall; at the same time the maximum increases until the interface almost touches the upper wall (this occurs at around $t = 50$; see also figure 1c,d). At later times the interfacial minimum and maximum settle down to a near-constant value; in fact they exhibit small-amplitude and apparently random fluctuations approximately a mean level, as can be seen from figure 3(d,e). This irregular large-time behaviour is reminiscent of the chaotic dynamics seen in the evolution of thin films (e.g. Kawahara 1983; Kawahara & Toh 1988; Kalogirou & Papageorgiou 2016). We explain this by noting that at large times the near-saturated state features a thin film of the lower fluid over much of the domain, and a thin film of the upper fluid confined between the top of the finger and the upper wall. The evolution of these thin films can be described by Kuramoto–Sivashinsky-type equations (see Appendix C and the related studies by Hooper & Grimshaw (1985), Charru & Fabre (1994), Tilley *et al.* (1994) and Kalogirou

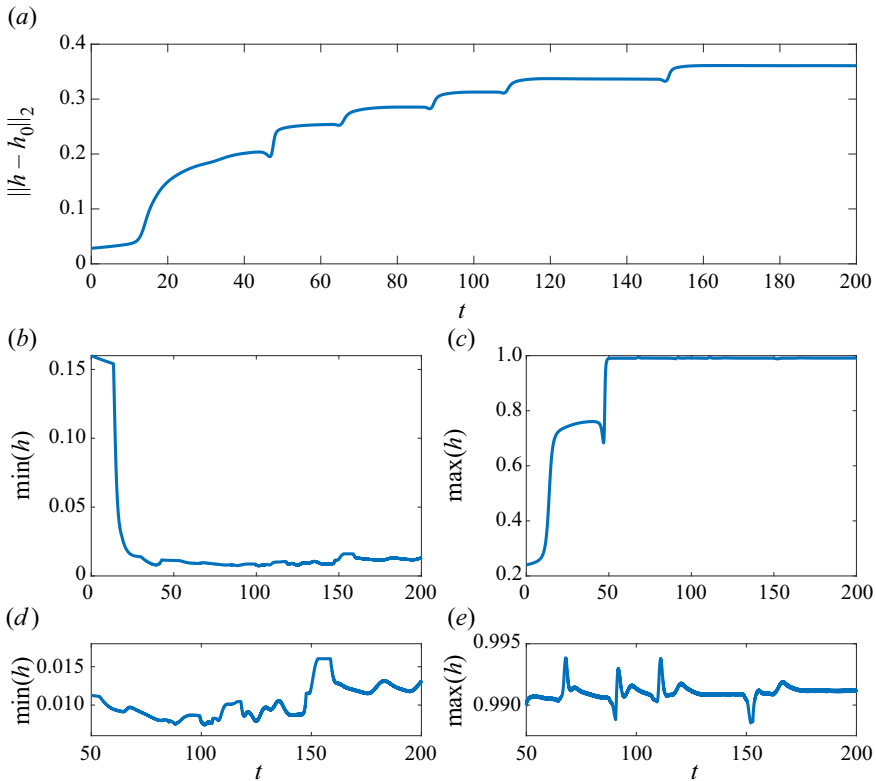


Figure 3. (a) Time evolution of interfacial solution norm, (b,c) interfacial minimum and maximum, including (d,e) a close-up evolution at later times of the simulation. Parameter values for h_0 , m , C , B remain the same as in figure 1.

et al. (2016)), which are well known for demonstrating chaotic behaviour (Papageorgiou, Maldarelli & Rumschitzki 1990). Both films are linearly unstable with a growth rate of the order of 10^{-3} ; its small size is attributable to the h_0^3 and $(1 - h_0)^3$ terms in the growth rate formula (B2). In related studies where the flow evolves from a static initial state, the fluid film tends to approach the wall in infinite time (Tseluiko & Papageorgiou 2007). Such a touch-down scenario appears to be absent here, and we believe the near saturation combined with thin-gap chaotic dynamics is connected with the background shear flow. In Appendix D we provide an analytical argument to support the numerical results seen in figures 1 and 3, in particular that the solution remains bounded such that $0 < h < 1$ for all time.

The final interfacial wave profile in figure 1(f), also shown in figure 4(a), features a capillary ridge and a depression on the top-right and the bottom-right part of the finger, respectively (these features are more obviously seen in the sketch in figure 11; see also in figure 13b). The interfacial velocity, shown with a red thin line in figure 4(a), becomes large in magnitude at the two points x_1 and x_2 where the interface is closest to each wall (similar behaviour was observed in Papageorgiou, Petropoulos & Vanden-Broeck (2005), Wang *et al.* (2009) and Barannyk *et al.* (2015)). To understand the source of these peaks we plotted the magnitude of the various terms that define the interfacial velocity in (A8) to determine which term dominates. We found that the \mathcal{F} term, defined in (2.8d), experiences (positive or negative) peaks as can be seen in figure 4(b), but these are most pronounced

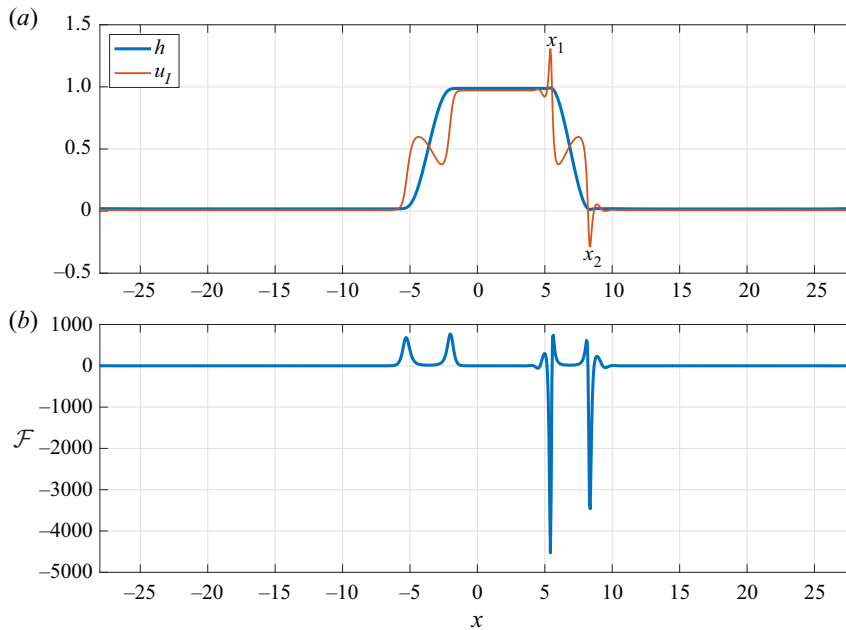


Figure 4. (a) Profile h of the interfacial wave (blue line) and interfacial horizontal velocity $u_I = u|_{y=h}$ (red line) and (b) term $\mathcal{F} = C^{-1}(Bh_x + h_{xxx})$ which dominates in the pressure gradient distribution, plotted at time $t = 200$. Parameter values for h_0, m, C, B are the same as in figure 1. The interfacial velocity is seen to become large in magnitude at the two points x_1 and x_2 where the interface takes the form of a capillary ridge or depression and is closest to the upper/lower channel walls. This is accompanied by a drop in the pressure gradient as evident by the dips in the profile of term \mathcal{F} .

where the interface is closest to each wall (i.e. at the points labelled as x_1 and x_2). We note that the \mathcal{F} term is related to F_χ in (A7b) and that this term dominates over the other terms in the pressure gradient expression (A11). The large negative peaks in the profile of \mathcal{F} lead to large negative spikes in pressure gradient, which drives the rapid flow near the walls (note that the flat parts of the \mathcal{F} curve are much smaller in magnitude, on the scale shown, but not constant).

3.2. Physical discussion

Intuition might suggest that the action of gravity will lead to the heavier fluid displacing the lower, lighter fluid. In a static configuration for which there is no preference for flow to the right or left, one would anticipate that a localised interfacial disturbance will tend to migrate upwards as fluid is drawn in from either side by hydrostatic force. Since the shear flow removes the left/right symmetry, the possibility arises of a finite-amplitude travelling wave that is sustained by a tripartite combination of shear, gravity and surface tension. Indeed, this has been demonstrated in the weakly nonlinear regime by Babchin *et al.* (1983). Examples of fully nonlinear waves in related unstably stratified problems include travelling waves on fluid films flowing down the underside of an inclined plane – see, for example, Kofman *et al.* (2018) and Zhou & Prosperetti (2022).

Considering moderate- to large-amplitude waves, we now examine more closely one of the travelling-wave solutions obtained as the large time limit of the initial value problem for the lubrication model equation (2.7) solved in § 3. In figure 5 we show the final-state interfacial profile when $B = 0.1$ together with the corresponding streamline

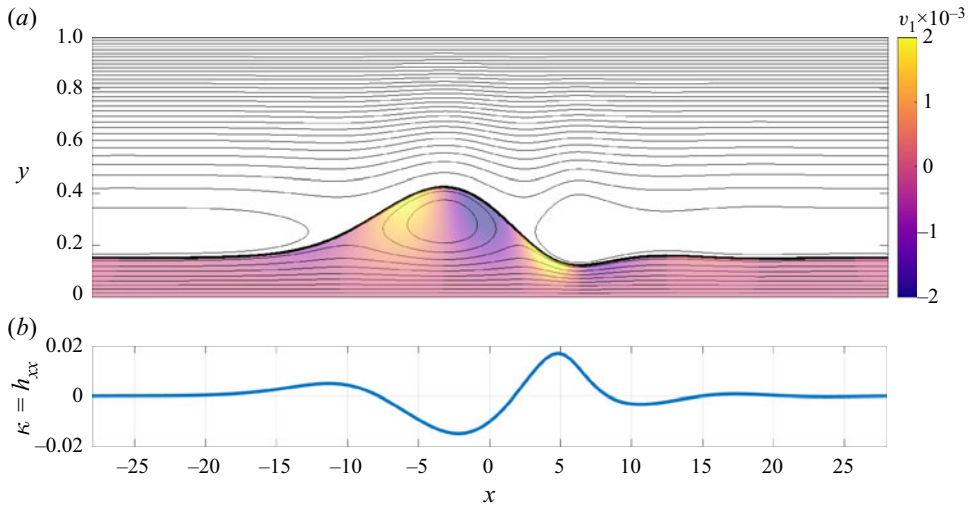


Figure 5. (a) Flow configuration and (b) interfacial curvature for $B = 0.1$ and parameters h_0, m, C fixed to the same values as in figure 1. In (a), the colour corresponds to the vertical velocity v_1 in the lower fluid, the thick line indicates the location of the interface and thin lines shown within the fluids are the streamlines.

pattern in a frame of reference that is travelling at the wave speed. Figure 6 shows a more highly deformed interfacial profile computed for $B = 0.4$. We note the striking qualitative similarity between the interfacial profile seen in figure 5 and that computed for a viscous film flowing on the underside of an inclined plate (see e.g. Kofman *et al.* 2018; Zhou & Prosperetti 2022).

The speed of the travelling frame is 0.18 for figure 5 and 0.465 for figure 6, both of which values are smaller than the upper wall speed, which is unity according to our non-dimensionalisation. Consequently, in both figures the flow is from right to left in the lower part of the channel and from left to right in the upper part of the channel. Focusing on the results in figure 5, located in the main part of the upward bulge in the lower fluid is an eddy with fluid circulating in the clockwise direction. Critically, the interface is not symmetric about the vertical line through the eddy centre. The fluid is drawn upward on the left-hand side of the eddy by hydrostatic force. On the right-hand side of the eddy the large curvatures that occur around $x = -2.5$ and $x = 5$ suggest that the capillary force is sufficiently strong to combat the hydrostatic effect and to drive the fluid downwards. The whole structure is sustained by the background shear flow which flushes the rest of the lower fluid away to the left.

For fairly small Bond number, the effect of surface tension is relatively strong and only reasonably mild interfacial curvature is needed to provide the necessary capillary pressure to support the eddy motion. For larger Bond number the relative effect of surface tension is weaker and much larger curvatures are needed to provide the necessary capillary pressure. Thus we see the notably sharper features in the interfacial profile for $B = 0.4$ in figure 6 at approximately $x = 17$ and $x = 21$, and the much stronger curvatures at the same locations, roughly a factor of ten larger than the corresponding values for the $B = 0.1$ case. Interestingly, the flow structure is more complex for the larger Bond number. There are many stagnation points within a single flow period: eight are located at the centre of eddies (note the four very slender eddies adjacent to the interface, which can be seen in

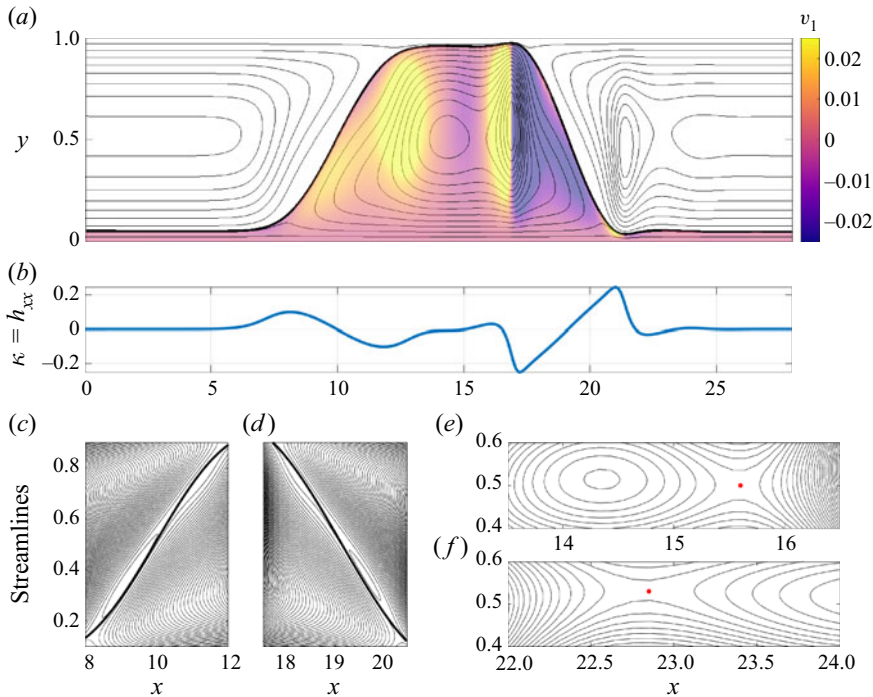


Figure 6. (a) Flow configuration and (b) interfacial curvature for $B = 0.4$ and parameters h_0, m, C fixed to the same values as in figure 1. The colour in (a) corresponds to the vertical velocity v_1 in the lower fluid. In (a,c-f), the thick line indicates the location of the interface and the thin lines shown within the fluids are the streamlines. Two clockwise-moving eddies exist in each fluid (panel a), and the streamlines are seen to cross at two stagnation points at $(x, y) = (15.6, 0.5)$ and $(22.85, 0.53)$, indicated by red dots in (e,f). Near the transition regions where the interface ascends/descends from one wall to the other, a total of four smaller counterclockwise-moving eddies are generated due to the draught from the surrounding fluids, as shown in (c,d).

figure 6(c,d), two more are located at local saddle points in the streamline pattern evident in figure 6(e,f) and several others are located on the interface itself.

3.3. Travelling-wave solutions

The results of the numerical simulation discussed in the previous section indicated that the interface evolves into a travelling wave. Although the flow was found to be chaotic in the narrow gaps at the walls, this does not significantly affect the rest of the wave profile so that overall the interfacial travelling wave propagates with approximately fixed form and constant speed in the direction of the background shear flow. Motivated by this, in this section we seek travelling-wave solutions to the evolution equation (2.7) using the continuation software AUTO-07p (Doedel & Oldman 2009). Introducing the travelling-wave coordinate $\xi = x - ct$, with wave speed $c > 0$, equation (2.7) becomes

$$-ch_\xi + q_\xi = 0. \tag{3.2}$$

Assuming steady flow in the travelling-wave frame, we take the total flow rate Q to be constant.

To prepare the ground for the computations in AUTO, we define the scaled independent variable $X = (\xi + L)/(2L)$, so that $X \in [0, 1]$, and rewrite (3.2) as the first-order system

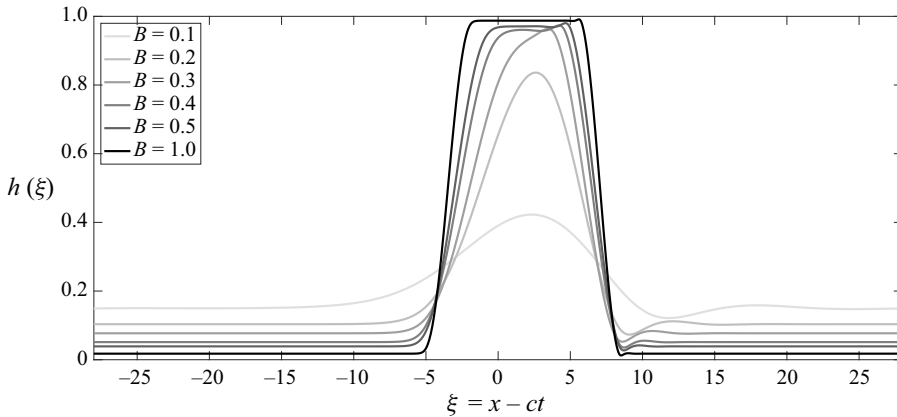


Figure 7. Interfacial travelling-wave profiles computed using AUTO for various values of B . The parameters h_0, m, C are fixed to the same values as in figure 1.

of ordinary differential equations $U_X = 2LA(U)$, where

$$U \equiv (U_1, U_2, U_3, U_4) \equiv (h, h_X, h_{XX}, h_{XXX}) \quad \text{and} \quad \mathcal{A}(U) \equiv (U_2, U_3, U_4, \mathcal{N}(U)). \tag{3.3a,b}$$

The nonlinear function $\mathcal{N}(U)$ in (3.3a,b) is found by rearranging equation (3.2) for h_{XXX} ; see also the expression for q in (2.7b) and the definition of \mathcal{F} in (2.8d). Periodic boundary conditions are imposed on h, h_X, h_{XX} . Three integral constraints are imposed to fix the volume of each fluid in a domain period, to break the translational invariance of the system (Sandstede 2002; Champneys & Sandstede 2007) and to enforce the zero-pressure-drop condition (A12). The parameter continuation is initiated close to the bifurcation point for small-amplitude periodic waves using the approximate solution $h(X) = h_0 + 10^{-3} \cos(2\pi X)$. The remaining parameters are determined so that the initial guess is close to neutral stability, according to predictions from linear theory (see Appendix B).

The number of free parameters in the continuation is determined by the relation $N_{cont} = N_{bc} + N_{int} - N_{dim} + 1$, where N_{bc} is the number of boundary conditions, N_{int} is the number of integral constraints and N_{dim} is the size of the system (Doedel & Oldman 2009). Here we have $N_{bc} = N_{int} = 3$ and $N_{dim} = 4$ (cf. (3.3a,b)), and hence $N_{cont} = 3$. We perform continuation in terms of the travelling-wave speed c , the flow rate Q and one other geometrical or physical parameter, such as the (half) domain length L or the undisturbed lower fluid thickness h_0 , while holding the rest of the parameters fixed.

Interfacial wave profiles obtained for different values of B are shown in figure 7 (the parameters h_0, m and C are set to the same values as in the previous section). Evidently the interface forms an increasingly pronounced finger as the Bond number increases. This results in a near segregation of the two fluids as the finger almost touches the walls at sufficiently large B . This is consistent with the time-dependent calculations of the previous section. In fact the profile for $B = 1$ is almost identical to the final wave state in figure 1(f), the only difference being that the thin-film regions near each wall are in the present case flat and steady. The capillary ridge and the depression at the leading edge of the finger are also apparent.

Figure 8 shows the variation of the travelling-wave speed c and the flow rate Q with the Bond number B , for different values of the undisturbed lower fluid thickness h_0 , capillary

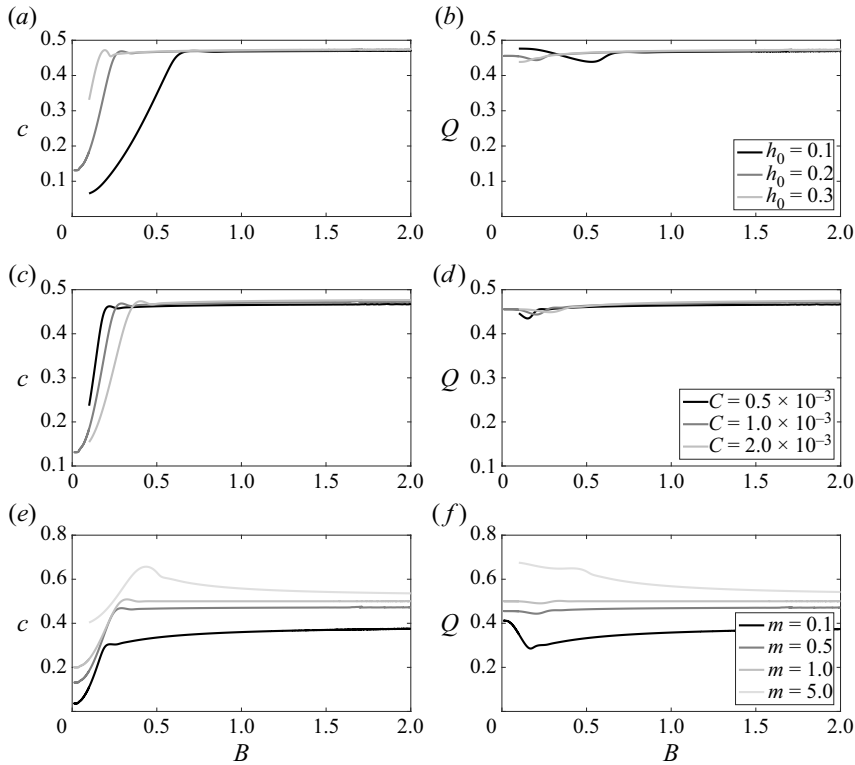


Figure 8. Variation of wave speed c and flow rate Q with Bond number B . The various curves shown are obtained for different values of (a,b) undisturbed lower fluid thickness h_0 , (c,d) capillary number C or (e,f) viscosity ratio m , as quoted in the respective legends (legends refer to both panels in the same row). Unless given in the legends, parameters h_0 , m , C take the same values as in figure 1.

number C and viscosity ratio m . Strikingly, for sufficiently large Bond number, both c and Q reach a plateau at the same limiting value. Furthermore, this limiting value increases with m but seems to be independent of both h_0 and C . Reducing h_0 delays the approach to the plateau, i.e. the wave speed becomes constant at a larger value of the Bond number. These results may be used to corroborate the comments made in the previous section on finger merging. From figure 8(a) it is clear that c depends strongly on h_0 before the plateau is attained. In a domain of fixed length $2L$, increasing h_0 increases the volume of the lower fluid leading to a taller finger. According to figure 8, roughly speaking c increases with h_0 so that a taller finger travels faster. Once h_0 is sufficiently large for the travelling wave to (almost) touch the upper wall, the finger widens as h_0 increases but the wave speed remains approximately constant.

3.4. Direct numerical simulations

Thus far our observations have been based on solutions to the model long-wave evolution equation (2.7). We have also considered values of the Bond number at which, strictly speaking, the model equation is outside of its range of validity (see the derivation in Appendix A). To provide some reassurance that our results are nonetheless relevant to a real flow, in this section we consider the full system (2.1), (2.3) and (A4) with no long-wave approximation. We solve this system numerically using the finite-element object-oriented

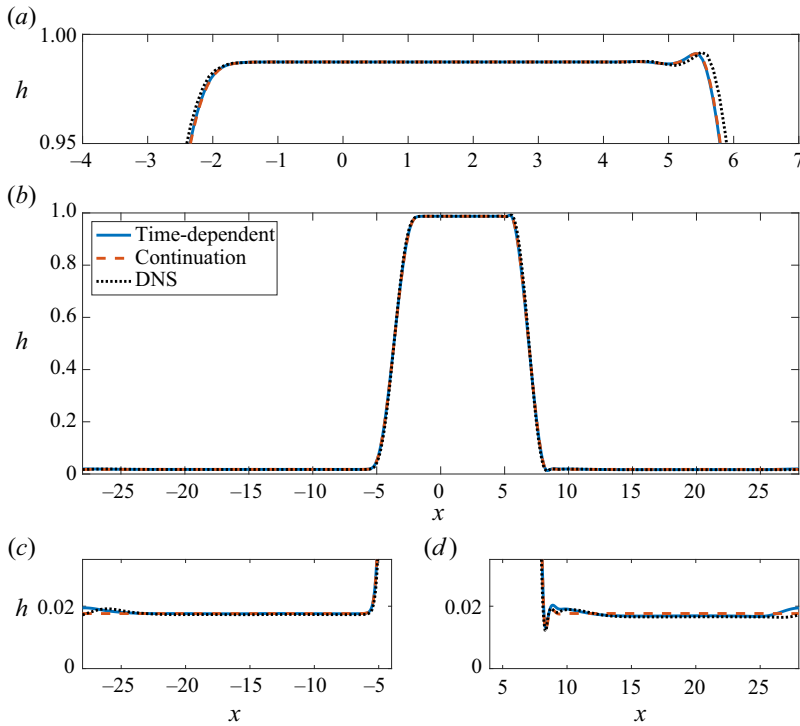


Figure 9. Comparison of interfacial profiles obtained from time-dependent calculations of the lubrication model, travelling-wave calculations of the same model and DNS of the Navier–Stokes equations. Each solution has been shifted to the right by an appropriate distance for better visualisation. The solution over the whole computational domain is shown in (b) with magnifications thereof illustrated in (a,c,d). Parameter values for h_0, m, C, B are the same as in figure 1.

multi-physics library oomph-lib (Heil & Hazel 2006a,b). The flow set-up is otherwise the same and we again start our simulations from the initial condition (3.1). Some additional details about the numerical implementation in oomph-lib are provided in Appendix E.

Generally speaking the interfacial displacement evolves in time in a manner similar to that predicted by the lubrication model. For sufficiently large Bond number this includes the early finger formation, the ensuing merging dynamics and the subsequent near-wall touch-down/touch-up behaviour. The ultimate fully merged profile comprising a single wide finger is shown in figure 9. Superimposed onto this profile is that found from the travelling-wave solution to the lubrication model (cf. § 3.3) and the large-time profile obtained from the time-dependent simulation of the lubrication model (cf. § 3.1). Despite the moderate size of the Bond number (here $B = 1$ and the lubrication model strictly requires $B \ll 1$) there is excellent agreement between all three sets of results. The only minor discrepancies occur in the upper part of the finger which is slightly wider in the DNS profile (figure 9a), and in the thin film near to the lower wall (figure 9c,d) where small interfacial ripples are observed in both sets of time-dependent calculations.

Inspired by the good agreement seen in figure 9 between model results and DNS, we performed extensive numerical simulations for a range of Bond numbers to establish the predictive power of the model. A comparison between numerical results obtained from time-dependent simulations of the model evolution equation (2.7) and DNS can be found in figure 10. In figure 10(a), the maximum absolute error is shown as a function of the Bond

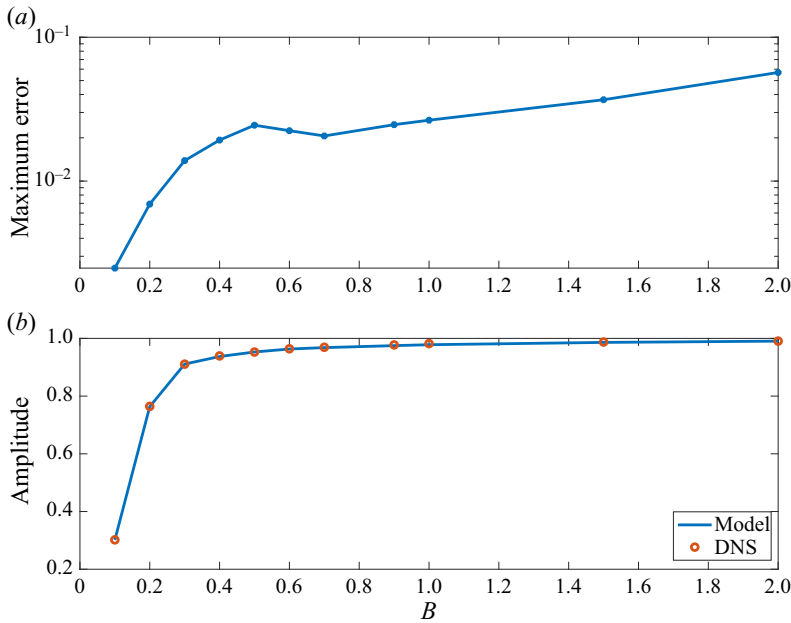


Figure 10. Comparison between numerical results obtained from time-dependent simulations of the model evolution equation (2.7) and DNS, for various Bond numbers. (a) Maximum absolute error found by calculating the difference between the two final-time interfacial profiles (model and DNS). (b) Solution amplitude found by taking the difference between the interfacial maximum and minimum at the final time. The parameters h_0 , m , C are fixed to the same values as in figure 1.

number, found by calculating the difference between the two final-time interfacial profiles. An overall trend of growing error for increasing Bond number is evident, indicating that the model will eventually (for much larger B) not be able to capture the ‘true’ dynamics. Figure 10(b) demonstrates that the amplitude of the two solutions is almost identical for all Bond numbers considered. For $B \gtrsim 0.4$, the interfacial structure almost touches both channel walls and the amplitude approaches the value 1 (cf. figure 8a). This allows us to conclude that the apparent increase in error at higher Bond numbers is mainly due to width disparity between the fingers, similar to that seen in figure 9(a).

4. Asymptotic analysis for large Bond number

Encouraged by the results in § 3, and in a bid to further understand the plateauing behaviour seen in figure 8, we now present an asymptotic analysis of the fully merged large-time travelling-wave state in the limit of large Bond number using the lubrication model.

We start by integrating equation (3.2) and using the definition of the flux in (2.7b), giving

$$q = \mathcal{D}^{-1} \left(mh^2 H_1 + \frac{1}{3} h^3 (1-h) H_2 \mathcal{F} \right) = ch - \mathcal{C}, \quad \text{for some constant } \mathcal{C}, \quad (4.1)$$

where the first term on the right-hand side is the additional flux in the lower layer introduced by the shift in reference frame. Seeking a solution in the limit $B \rightarrow \infty$ to support the results found in §§ 3.1–3.3, we divide the expected wide-finger solution into a number of asymptotic regions as shown in figure 11. This includes two transition regions

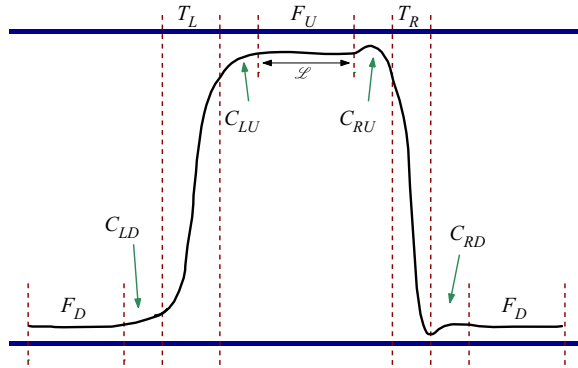


Figure 11. Sketch of the saturated interfacial profile of width \mathcal{L} , with the various asymptotic regions. The dashed vertical lines indicate locations of matching between solutions in the different regions. Key to region names: T_R/T_L , right/left transition regions; F_D/F_U , down/up flat-film regions; $C_{RD}/C_{RU}/C_{LD}/C_{LU}$, right/left and down/up connection regions.

T_L, T_R in which the profile ascends/descends from one wall to the other (here, subscripts L and R denote ‘left’ and ‘right’); two flat thin-film regions F_D and F_U (here, subscripts D/U mean down/up); and four connection regions $C_{RD}, C_{RU}, C_{LD}, C_{LU}$ that match the right/left transition regions to the down/up thin-film regions.

4.1. Transition regions T_R and T_L

We suppose there exist two transition regions in which (asymptotically) the two walls are connected to each other by a section of the interface which meets them at zero contact angle. In both of these regions the interface has a relatively steep slope. We seek a solution in the form

$$h = \mathcal{H}(\zeta), \quad \text{with} \quad \xi = B^{-1/2}\zeta \quad \text{in } T_R; \quad \xi = -\mathcal{L} - B^{-1/2}\zeta \quad \text{in } T_L, \quad (4.2a-c)$$

where \mathcal{H} is to be found, $\zeta = O(1)$ and \mathcal{L} is the width of region F_U (see figure 11). We note that the scaling of $B^{-1/2} \ll 1$ for the ξ coordinate was chosen to retain the effect of surface tension at leading order, by ensuring the balance of the two terms on the right-hand side of (2.8d). In the coordinate rescalings (4.2b,c), the origin of ξ is assumed to be in region T_R and hence (4.2c) is essentially a shift of (4.2b) by a distance \mathcal{L} . The value of \mathcal{L} can be estimated analytically by noticing that almost all the volume of the lower fluid is included in the finger. The volume of the finger is approximately \mathcal{L} (the dimensionless height of the channel is 1), and this should be equal to the lower fluid volume in the undisturbed state. Therefore at leading order, $\mathcal{L} = 2Lh_0$, where $2L$ is the domain length and h_0 is the undisturbed lower fluid height.

We assume that m, C and Q are of order 1, and that $c = O(1)$ and $\mathcal{C} = o(B^{3/2})$ (these latter scalings will be confirmed later). Then (4.1) becomes at leading order

$$\mathcal{H}_\zeta + \mathcal{H}_\zeta \zeta = 0, \quad (4.3)$$

noting that \mathcal{D} and H_2 are positive for $0 < \mathcal{H} < 1$. Assuming a solution in which the interface meets each wall with zero contact angle, then

$$\mathcal{H} = \frac{1}{2}(1 - \sin \zeta), \quad \text{over} \quad -\frac{\pi}{2} < \zeta < \frac{\pi}{2}. \quad (4.4)$$

For later reference, it is important to note that

$$\mathcal{H} \sim \frac{1}{4} \left(\zeta - \frac{\pi}{2} \right)^2, \quad \text{as } \zeta \rightarrow \frac{\pi}{2}, \quad (4.5a)$$

$$\mathcal{H} \sim 1 - \frac{1}{4} \left(\zeta + \frac{\pi}{2} \right)^2, \quad \text{as } \zeta \rightarrow -\frac{\pi}{2}. \quad (4.5b)$$

In both transition regions the limit $\zeta \rightarrow \pm\pi/2$ corresponds to approaching the film near the lower/upper wall, respectively.

4.2. Flat-film regions F_D and F_U

In the flat thin-film regions against the lower/upper walls (these regions lie outside/inside the finger), the film is of approximately uniform thickness and we take, respectively,

$$h = B^{-1}H_D \quad \text{or} \quad h = 1 - B^{-1}H_U, \quad (4.6a,b)$$

where H_D and H_U are both constant. The scaling of B^{-1} is chosen for matching purposes as we will see later. In region F_D , (2.7b) implies $q \sim B^{-2}$, and so the right-hand side dominates in (4.1) and the flat-film thickness is found to be

$$H_D = \frac{\hat{\mathcal{C}}}{c}, \quad (4.7)$$

where we have defined

$$\mathcal{C} = B^{-1}\hat{\mathcal{C}}. \quad (4.8)$$

In region F_U , we expand q in terms of B^{-1} , apply the scaling (4.8) in (4.1) and disregard terms of $O(B^{-2})$, resulting in

$$Q - B^{-1}H_U = c - B^{-1} \left(cH_U + \mathcal{C} \right). \quad (4.9)$$

Hence the appropriate balance at $O(1)$ and $O(B^{-1})$ gives, respectively,

$$Q = c \quad \text{and} \quad H_U = \frac{\mathcal{C}}{1-c} = \frac{c}{(1-c)}H_D, \quad (4.10a,b)$$

on using (4.7). The leading-order relationship between c and Q in (4.10a) has already been noted in the results of figure 8.

4.3. Connection regions C_{RD} and C_{RU}

Here we write

$$h = B^{-1}\tilde{H}(z) \quad \text{or} \quad h = 1 - B^{-1}\hat{H}(z), \quad \text{and} \quad \xi = \pm \left(B^{-1/2}\frac{\pi}{2} + B^{-1}z \right), \quad (4.11a-c)$$

where (4.11a,b) are introduced in regions C_{RD}/C_{RU} (near the lower/upper walls), respectively, and the plus/minus signs in (4.11c) apply in the respective regions C_{RD}/C_{RU} .

Taking Taylor expansions with respect to B^{-1} in the various functions used to define the flux q in (2.7b), and substituting in (4.1), provides the leading-order balance in each connection region. In particular, accounting for (4.8), in region C_{RD} we find at $O(B^{-1})$

$$\frac{1}{3C} \tilde{H}^3 \tilde{H}_{zzz} = c\tilde{H} - \hat{\mathcal{C}}, \tag{4.12a}$$

and in region C_{RU} we recover (4.10a) at $O(1)$, while at $O(B^{-1})$ we get

$$\frac{1}{3mC} \hat{H}^3 \hat{H}_{zzz} = (1 - c)\hat{H} - \hat{\mathcal{C}}. \tag{4.12b}$$

Making use of (4.7) and (4.10b), we rescale by writing $\{\tilde{H}, \hat{H}\} = \{H_D, H_U\}H$ and $z = \beta_{\{D,U\}}Z$, where $\beta_D = H_D/(3Cc)^{1/3}$ and $\beta_U = H_U/(3mC(1 - c))^{1/3}$. Then (4.12) both reduce to the Landau–Levich equation (Landau & Levich 1942, see also Bretherton 1961)

$$H''' = \frac{H - 1}{H^3}, \tag{4.13}$$

where a prime denotes a derivative with respect to Z .

The far-field conditions follow by matching to the solution in transition region T_R and to the flat-film solution at the walls. Reconciling the scalings (4.2b) and (4.11c), and using (4.5) and (4.6), the required matching conditions in regions C_{RD}/C_{RU} are

$$H \sim \frac{1}{2} \mathcal{A}_{\{D,U\}} Z^2 \quad \text{as } Z \rightarrow -\infty \quad \text{and} \quad H \sim 1 \quad \text{as } Z \rightarrow \infty, \tag{4.14a,b}$$

where

$$\mathcal{A}_D = \frac{\beta_D^2}{2H_D} \quad \text{and} \quad \mathcal{A}_U = \frac{\beta_U^2}{2H_U}. \tag{4.15a,b}$$

The first and second conditions in (4.14a,b) effect the matches with the transition region T_R and with the flat thin-film regions F_D, F_U , respectively. The connecting region problems near the right transition region thus require the solution of the Landau–Levich equation (4.13) subject to the matching conditions (4.14a,b). This problem appears in a number of related studies including the dragging of a liquid by a moving plate (Landau & Levich 1942), the motion of long bubbles in horizontal tubes (Bretherton 1961) and the capillary draining of annular films in horizontal tubes (Hammond 1983; Lister *et al.* 2006) and vertical tubes (Jensen 2000). It has a one-parameter family of solutions, meaning that $\mathcal{A}_{\{D,U\}}$ cannot be determined at this stage.

4.4. Connection regions C_{LD} and C_{LU}

Working as in the previous section, we write

$$h = B^{-1} \tilde{\mathcal{H}}(z) \quad \text{or} \quad h = 1 - B^{-1} \hat{\mathcal{H}}(z), \quad \text{and} \quad \xi = -\mathcal{L} \pm \left(-B^{-1/2} \frac{\pi}{2} + B^{-1} z \right), \tag{4.16a-c}$$

where \mathcal{L} was introduced in (4.2c). The scalings (4.16a,b) are applied in regions C_{LD}/C_{LU} (near the lower/upper walls), respectively, and the plus/minus signs in (4.16c) apply in the respective regions C_{LD}/C_{LU} .

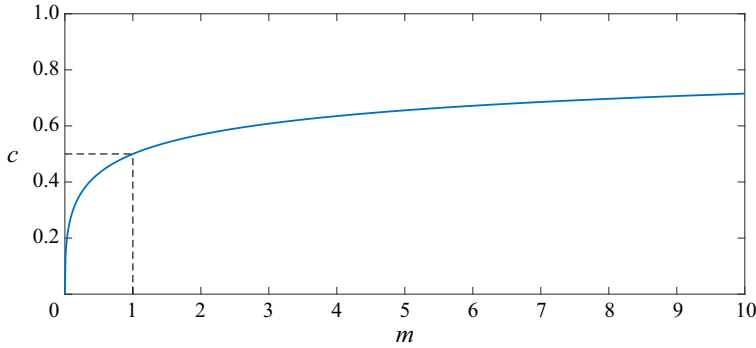


Figure 12. Variation of the interfacial wave speed c against the viscosity ratio m , according to the asymptotic result in (4.18).

Introducing the same scalings as before, $\{\mathcal{H}, \tilde{\mathcal{H}}\} = \{H_D, H_U\}H$ and $z = \beta_{\{D,U\}}Z$, we again obtain the Landau–Levich equation (4.13). The matching conditions are

$$H \sim \frac{1}{2}\mathcal{A}_{\{D,U\}}Z^2 \quad \text{as } Z \rightarrow \infty \quad \text{and} \quad H \sim 1 \quad \text{as } Z \rightarrow -\infty. \quad (4.17a,b)$$

The asymptotic problem given by (4.13) and (4.17a,b) admits a unique solution and therefore $\mathcal{A}_D = \mathcal{A}_U$. We find numerically that these constants are equal to 0.643, which agrees with the value quoted elsewhere in the literature (e.g. Bretherton 1961; Jensen 2000; Lister *et al.* 2006).

4.5. Comparison with numerical solutions

Since $\mathcal{A}_D = \mathcal{A}_U$, it follows from (4.15a,b) that an explicit formula can be obtained for the wave speed at leading order (using also the definitions of H_D and H_U from (4.7) and (4.10b)), given by

$$c = \frac{m^{2/5}}{1 + m^{2/5}}. \quad (4.18)$$

It is surprising that c depends only on the viscosity ratio, but this is in line with the results presented in § 3.3, in particular figure 8. The relationship (4.18) is plotted in figure 12. The wave speed varies rapidly with m when $m < 1$ and the lower fluid is the more viscous. Note that $0 < c < 1$ and so the wave speed is less than the wall speed (which has been used to non-dimensionalise velocities); in particular $c = 1/2$ when $m = 1/2$ so that the wave propagates at half the wall speed for equal-viscosity fluids. These remarks agree with the results in figure 8.

Since $\mathcal{A}_D = \mathcal{A}_U = 0.643$, it follows that the as yet undetermined constant $\hat{\mathcal{C}}$ is given by

$$\hat{\mathcal{C}} = 2.675 C^{2/3} c^{5/3}, \quad (4.19)$$

where c is given by (4.18). This result may be combined with (4.6), (4.7) and (4.10b) to yield an estimate for the thin-film thickness in regions F_D, F_U for a particular value of B .

We conclude this section by comparing the predictions of the present asymptotic analysis with numerical solutions of the lubrication model and of the full equations via DNS. To facilitate this comparison, we fix the parameters to the same values that were used in the numerical computations in § 3, namely $h_0 = 0.2$, $m = 0.5$, $C = 10^{-3}$,

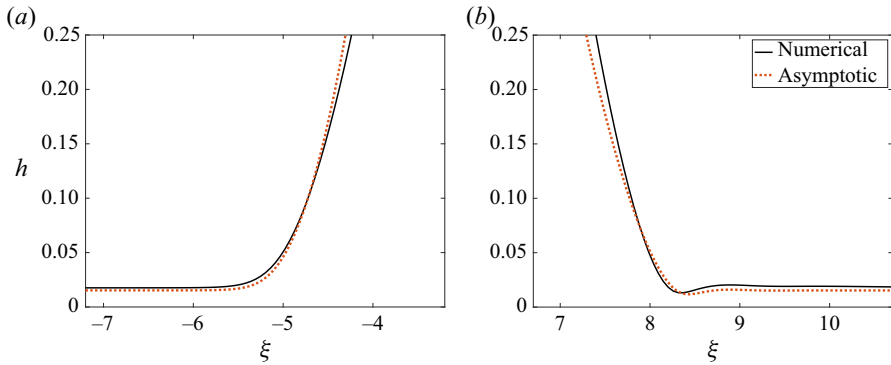


Figure 13. Solution to the asymptotic problem in the (a) left and (b) right connection regions, plotted for the same parameter values used in previous figures ($h_0 = 0.2$, $m = 0.5$, $C = 10^{-3}$, $B = 1$), and shown with red dashed curves. The black solid curves correspond to the time-dependent results. The asymptotic results have been rescaled back to the original variables, $h = h(\xi)$, by using the appropriate values for $\beta_{\{D,U\}}$ and scalings in (4.11), and have been also shifted horizontally in order to match the spatial location of the connection regions as seen in figure 1(f).

and we take a moderate value for the Bond number such as $B = 1$. Setting $m = 0.5$ in (4.18) yields the leading-order prediction for the wave speed $c = 0.43$. The numerically computed speed for the lubrication model is approximately $c = 0.4725$; this was obtained from a time-dependent simulation of the lubrication model (2.7) and it was confirmed by a travelling-wave calculation as described in § 3.3; see, in particular, figure 8. The corresponding wave speed obtained from DNS is approximately $c_{DNS} = 0.4723$. Once again we note that the lubrication model agrees well with full DNS even for Bond numbers outside its strict range of validity.

Using these results and taking the same parameter values in (4.19), (4.7), (4.10b) and then (4.6), we find the individual film thicknesses to be $h_{FD} = 0.015$ and $h_{FU} = 0.012$ near the down/up walls, respectively, while the numerically computed values from the lubrication model are 0.0176 and 0.0126, respectively, and the corresponding DNS values are approximately 0.0175 and 0.0127. Clearly the results obtained from simulations of the lubrication model and DNS are almost identical, and they are in good agreement with the asymptotic results.

Finally we compare the numerical solution of the asymptotic problem in each connection region with that obtained via a time-dependent simulation of the lubrication model. Numerically solving the Landau–Levich equation (4.13) with far-field conditions (4.14a,b) or (4.17a,b) gives the solutions shown with the red curves in figure 13 (the results have been scaled back to the original variables). The solution obtained from time-dependent simulations is superimposed with black curves (this is the same profile shown in figure 1f), providing good agreement between the two sets of results.

5. Conclusions

We have considered the RT instability that arises at the interface between two immiscible viscous fluids in a channel that is undergoing a shearing motion due to the translation of the upper wall. We have derived a nonlinear lubrication equation that is appropriate for describing the evolution of the fluid–fluid interface on the assumption that the wavelength of the interfacial disturbances is large in comparison with the channel height. For any positive Bond number, meaning that the fluids are unstably stratified and RT

instability is present, a small-amplitude perturbation to the initially flat interface grows to develop a highly nonlinear structure. Numerical computations performed assuming periodic boundary conditions, and on the assumption that there is no pressure drop across one period, demonstrated the appearance of a pronounced finger-like pattern with the number of fingers in one period accurately predicted by linear stability theory. The fingers in general have different heights and travel at different speeds (taller fingers travel faster) so that inter-finger collisions and merging events occur. As merging continues the number of fingers gradually reduces leaving finally a residual finger which roughly encompasses all of the lower fluid volume. This behaviour is similar to the coarsening dynamics of roll wave structures propagating down an inclined plane (Chang *et al.* 2000; Razis *et al.* 2014). At sufficiently large Bond number the final finger spans the entire channel cross-section so that it essentially segregates the two fluids; the width of the finger is set by the initial volume ratio of the two fluids in the periodic domain. The finger propagates as a more-or-less fixed-form travelling wave, although thin-film coatings of each fluid adjacent to the channel walls are unsteady. Their highly irregular behaviour is reminiscent of the chaotic dynamics that characterises the evolution of thin films in certain parameter regimes (Kawahara 1983; Kawahara & Toh 1988; Kalogirou & Papageorgiou 2016). We have demonstrated analytically that touch-down/touch-up of the interface with the channel walls does not occur in finite time, and our numerics in fact indicate that the minimum gap almost saturates in time due to the presence of a base shear flow.

The existence of fully steady travelling-wave solutions was confirmed by a continuation procedure carried out using AUTO-07p (Doedel & Oldman 2009) in a moving reference frame. These calculations successfully reproduced the large-time interfacial profile attained in the unsteady simulations (overlooking the persistent chaotic behaviour in the thin-film regions). Furthermore they demonstrated that the wave speed and the total channel flux both reach a plateau as the Bond number is increased to a relatively large value (in fact roughly around $B = 1$), and that this plateau depends only on the size of the viscosity ratio. This behaviour was further investigated via a large-Bond-number asymptotic analysis that revealed the finer details of the post-coarsening final-state travelling wave and confirmed that the wave speed and channel flux approach the same value in the large- B limit. The asymptotic structure includes localised depression and capillary ridge features that occur in narrow connection regions close to the wall wherein the system is well approximated by the Landau–Levich equation (Landau & Levich 1942). In this regard our analysis resembles that presented by other authors for similar problems (e.g. Bretherton 1961; Hammond 1983; Jensen 2000; Lister *et al.* 2006).

Although we have focused our attention on relatively large values of the Bond number, our lubrication equation is formally only valid for small values of this parameter (in that case, smaller-amplitude travelling waves that do not straddle the whole channel height are achieved; see the light grey curve in figure 7 for an example using $B = 0.1$). With this in mind we have also carried out time-dependent simulations of the full Stokes equations. These were found to be in excellent agreement with the predictions of the lubrication model, even for moderate sized Bond number. Both qualitative and quantitative agreement was found, for example in the estimation of the final-state travelling-wave speed and the residual film thickness at the channel walls. For sufficiently large Bond number, the model predictions are not expected to accurately characterise the dynamics (cf. figure 10). In fact, for large enough Bond number we expect to see features such as interfacial break-up and droplet formation (Kalogirou, Cimpeanu & Blyth 2020).

The stability of the final travelling-wave states has not been addressed here directly. However, since for both the lubrication model and the full Stokes equations the waves

emerge as the large-time limit of an initial value problem, this suggests that they are stable to two-dimensional disturbances; although loss of stability to perturbations of wavelength greater than the length of our computational domain cannot be ruled out. The stability of the system to transverse perturbations, however, remains to be investigated (e.g. Mavromoustaki, Matar & Craster 2011). While in this paper we have focused on single-finger saturated states, multi-finger states can also be attained in unsteady simulations through particular choices of the initial condition, and these are the subject of our ongoing research. A further point of interest suggested by the asymptotic analysis of § 4 concerns the possibility of finding shock-like solutions wherein the interfacial level changes smoothly from one constant value to another from upstream to downstream in the manner of a hydraulic fall. It should be noted that the analysis of § 4 does not determine the width of the travelling wave, \mathcal{L} , this being set effectively by the volume ratio of the two fluids in the periodic domain. With this in mind, by extending the domain length to infinity, shock solutions of the kind computed for an inclined channel with stationary walls by Mavromoustaki *et al.* (2010), using the entropy-flux approach of Bertozzi, Münch & Shearer (1999), could presumably be constructed. This is left as a topic for future investigation.

Supplementary movie. Supplementary movie is available at <https://doi.org/10.1017/jfm.2022.1070>.

Acknowledgements. We thank Professor A. Hazel for the help with setting up the oomph-lib code which was used for the DNS.

Funding. This research received no specific grant from any funding agency, commercial or not-for-profit sectors.

Declaration of interests. The authors report no conflict of interest.

Author ORCIDs.

 A. Kalogirou <https://orcid.org/0000-0002-4668-7747>;

 M.G. Blyth <https://orcid.org/0000-0002-7480-4138>.

Appendix A. Derivation of the lubrication equation

A lubrication equation for the evolution of a disturbance at the interface can be derived by assuming that the wavelength of the disturbance is much larger than the channel height. This suggests a rescaling of the horizontal coordinate and the introduction of a slow time scale as follows:

$$\chi = \epsilon x, \quad \tau = \epsilon t, \quad \text{with } \epsilon \ll 1, \tag{A1}$$

where ϵ is the height-to-wavelength ratio and χ, τ are of $O(1)$. The flow velocities and pressures are expanded in the following manner (Tilley *et al.* 1994):

$$u_j = u_j^{(0)} + \epsilon u_j^{(1)}, \quad v_j = \epsilon v_j^{(0)} + \epsilon^2 v_j^{(1)}, \quad p_j = \epsilon^{-1} p_j^{(0)} + p_j^{(1)}. \tag{A2a-c}$$

The following rescaling for the Bond and capillary numbers is also introduced, in order to keep the effects of gravity and surface tension in the leading-order dynamics (e.g. Mavromoustaki *et al.* 2010):

$$B = \epsilon^2 \tilde{B}, \quad C = \epsilon^3 \tilde{C} \quad \text{with } \tilde{B}, \tilde{C} = O(1). \tag{A3}$$

Expansions (A2a–c) and rescalings (A1) and (A3) are substituted into the kinematic equation

$$h_t + \left(\int_0^{h(x,t)} u_1 \, dy \right)_x = 0 \quad \text{at } y = h(x, t), \quad (\text{A4})$$

the momentum and continuity equations (2.1), and the normal and tangential stress balances given in (2.3), yielding the leading-order system

$$m_j u_{jyy}^{(0)} - p_{j\chi}^{(0)} = 0, \quad \text{for } j = 1, 2, \quad (\text{A5a})$$

$$p_{jy}^{(0)} + \frac{r_j}{(r-1)} \frac{\tilde{B}}{\tilde{C}} = 0, \quad \text{for } j = 1, 2, \quad (\text{A5b})$$

$$u_{j\chi}^{(0)} + v_{jy}^{(0)} = 0, \quad \text{for } j = 1, 2, \quad (\text{A5c})$$

$$u_1^{(0)} = 0, \quad v_1^{(0)} = 0, \quad \text{at } y = 0, \quad (\text{A5d})$$

$$u_2^{(0)} = 1, \quad v_2^{(0)} = 0, \quad \text{at } y = 1, \quad (\text{A5e})$$

$$u_1^{(0)} = u_2^{(0)}, \quad \text{at } y = h(\chi, \tau), \quad (\text{A5f})$$

$$m u_{2y}^{(0)} - u_{1y}^{(0)} = 0, \quad \text{at } y = h(\chi, \tau), \quad (\text{A5g})$$

$$p_2^{(0)} - p_1^{(0)} = \frac{1}{\tilde{C}} h_{\chi\chi}, \quad \text{at } y = h(\chi, \tau), \quad (\text{A5h})$$

$$\int_0^h u_1^{(0)} \, dy + \int_h^1 u_2^{(0)} \, dy = Q(t). \quad (\text{A5i})$$

Integrating (A5b) in y gives

$$p_j^{(0)} = -\frac{r_j}{(r-1)} \frac{\tilde{B}}{\tilde{C}} y + P_j, \quad (\text{A6})$$

where the functions $P_j(\chi, \tau)$ are related to each other, via condition (A5h), as

$$P_2 = P_1 + F, \quad \text{where } F = \tilde{C}^{-1}(\tilde{B}h + h_{\chi\chi}). \quad (\text{A7a,b})$$

The momentum equations (A5a) can then be integrated in y twice to obtain

$$u_1^{(0)} = \frac{1}{2} y^2 P_{1\chi} + y A_1, \quad u_2^{(0)} = \frac{1}{2m} (y^2 - 1) P_{2\chi} + (y - 1) A_2 + 1, \quad (\text{A8a,b})$$

where the no-slip boundary conditions at the walls (A5d), (A5e) have been applied. The arbitrary functions $A_j = A_j(\chi, \tau)$ are determined by using the two conditions (A5f), (A5g), and then using (A7a). Their expressions simplify to

$$A_2 = \frac{1}{m} (A_1 - h F_\chi), \quad A_1 = \frac{2m - (1 + (m-1)h^2) P_{1\chi} - (h-1)^2 F_\chi}{2(1 + (m-1)h)}. \quad (\text{A9a,b})$$

The continuity equations (A5c) can be used to provide similar expressions for the leading-order vertical velocity perturbations; integrating in y and using the no-penetration

boundary conditions at the walls (A5d), (A5e), yields

$$v_1^{(0)} = -\frac{1}{6}y^3 P_{1\chi\chi} - \frac{1}{2}y^2 A_{1\chi}, \quad v_2^{(0)} = -\frac{1}{6m}(y^3 - 3y + 2)P_{2\chi\chi} - \frac{1}{2}(y^2 - 2y + 1)A_{2\chi}. \tag{A10a,b}$$

It remains to use the integral constraint (A5i) to determine the leading-order pressure gradient, finding

$$P_{1\chi} = \mathcal{D}^{-1} \left[-6m \left((m-1)h^2 - 2(m-1)h - 1 \right) + (h-1)^2 \left((m-1)h^2 + 2(1-2m)h - 1 \right) F_\chi - 12m((m-1)h + 1) Q(t) \right], \tag{A11}$$

where \mathcal{D} is defined in (2.8a). We note that the flow rate $Q(t)$ can be found by satisfying a periodicity condition on the pressure (Ooms *et al.* 1985; Blyth & Pozrikidis 2004; Kalogirou & Blyth 2020), e.g.

$$\int_{-L}^L P_{1\chi} dx = P_1(L, \tau) - P_1(-L, \tau) = 0, \tag{A12}$$

or equivalently fixing the pressure drop in the streamwise direction to be zero over a specified domain of length $2L$.

With the solution for $P_{1\chi}$ known from (A11), function A_1 and then A_2 can be found from (A9a,b) and finally $P_{2\chi}$ can be found using (A7a). The leading-order horizontal velocities in each fluid can then be obtained from (A8). The evolution of the interfacial displacement is found by inserting the leading-order horizontal velocity (A8a) into the kinematic equation (A4), and is given by

$$h_\tau + q_\chi = 0 \quad \text{with } q = \frac{1}{6}P_{1\chi}h^3 + \frac{1}{2}A_1h^2. \tag{A13}$$

The evolution equation (A13) can be scaled back to the original variables x, t and the result is given in (2.7), which also includes the original parameters B, C . We note that the expression for q in (2.7) is the same as that in (A13), but it is written in a different form for convenience.

Appendix B. Linear stability theory

The growth rate of (2.7) is found by writing $h = h_0 + A \exp(iKx + \sigma t) + \text{c.c.}$ (complex conjugate) for some small amplitude A . Here, σ is the growth rate which is generally a complex number and K is the wavenumber, assumed real. Substituting this expression into (2.7) yields

$$\sigma + iK\mathcal{D}(h_0)^{-1} \left(mh_0^2 H_1(h_0) + \frac{1}{3C}h_0^3(1-h_0)^3 H_2(h_0)(iKB - iK^3) \right) = 0. \tag{B1}$$

The growth rate is then provided by the real part of σ and is given by

$$\text{Re}(\sigma) = K^2(B - K^2) \frac{h_0^3(1-h_0)^3 H_2(h_0)}{3C\mathcal{D}(h_0)}. \tag{B2}$$

Since $0 < h_0 < 1$, and $\mathcal{D} > 0, H_2 > 0$, the growth rate is clearly positive if $K < K_c$, where the cut-off wavenumber is $K_c = \sqrt{B}$. The growth rate attains its maximum at the point where $\partial_K(\text{Re}(\sigma)) = 0$, which is located at $K_{max} = \sqrt{B}/2$.

Appendix C. Weakly nonlinear analysis

Writing $h(x, t) = \delta(H_0 + \delta H(x, t))$ in (2.7), with $\delta \ll 1$, $H_0 = O(1)$ is constant and $H = O(1)$, we find

$$\delta^2 H_t + \left[\alpha_1 H \delta^3 + (\alpha_2 H + \alpha_3 H^2) \delta^4 + (\alpha_4 H + \alpha_5 H^2 + \alpha_6 H_x + \alpha_7 H_{xxx}) \delta^5 + O(\delta^6) \right]_x = 0, \tag{C1}$$

where $\alpha_i = \alpha_i(H_0, m, Q(t))$ for $i = 1, \dots, 5$, and $\alpha_6 = H_0^3 B / (3C)$, $\alpha_7 = H_0^3 / (3C)$. The numerical evidence suggests that the flow rate Q is a constant in the large-time limit when the travelling-wave structure is reached (see figure 8), so we treat $Q(t)$ as a constant to leading order. The second term on the left-hand side can be then removed by taking a Galilean transformation of the form $\hat{x} = x - \delta \alpha_1 t$. A slow-time scale is introduced by $\hat{t} = \delta^2 t$, and the capillary number is rescaled as $C = \delta C_0$ (Kalogirou & Papageorgiou 2016), and so the evolution equation (C1) becomes at leading order

$$H_{\hat{t}} + \alpha H_{\hat{x}} + 2\alpha_3 H H_{\hat{x}} + \frac{H_0^3}{3C_0} (B H_{\hat{x}\hat{x}} + H_{\hat{x}\hat{x}\hat{x}}) = 0, \tag{C2}$$

where α is a time-dependent coefficient which depends on the first-order correction to $Q(t)$.

Appendix D. Boundedness of solutions

The results in § 3.1 suggest that when the interface gets close to one of the channel walls, then the \mathcal{F} term in (2.8d) dominates the evolution equation (2.7); cf. figure 4. To examine near-wall touch-down/touch-up, it is therefore sufficient to keep only the dominant terms in the evolution equation, which reduces to

$$h_t + \left(\frac{1}{3} h^3 (1 - h)^3 \mathcal{D}^{-1} H_2 \mathcal{F} \right)_x = 0, \tag{D1}$$

where we recall that $\mathcal{F} = C^{-1}(B h_x + h_{xxx})$. A similar equation has been obtained in related studies investigating the RT instability in thin viscous films (Yiantsios & Higgins 1989), also in the presence of electric fields (Tseluiko & Papageorgiou 2007; Anderson *et al.* 2017). In particular, if the interface is in the vicinity of the lower or upper wall, that is, $h \approx 0$ or $h \approx 1$, the evolution equation (D1) is similar to those previously derived by Tseluiko & Papageorgiou (2007) or Anderson *et al.* (2017), respectively, if the influence of electric fields is omitted in both of these studies.

Here we aim to prove that smooth solutions are uniformly bounded. We follow closely the proof of Tseluiko & Papageorgiou (2007) for an electrified film. We begin by defining the functional

$$E(h) = \frac{1}{2} C^{-1} \int_{-L}^L (-B h^2 + h_x^2) dx. \tag{D2}$$

This can be shown to be non-increasing in time, as follows:

$$\begin{aligned} \frac{dE}{dt} &= \int_{-L}^L C^{-1} (-Bhh_t + h_x h_{xt}) \, dx = \int_{-L}^L C^{-1} (Bh + h_{xx}) (-h_t) \, dx \\ &= \int_{-L}^L C^{-1} (Bh + h_{xx}) \left(\frac{1}{3} h^3 (1-h)^3 \mathcal{D}^{-1} H_2 \mathcal{F} \right)_x \, dx \\ &= - \int_{-L}^L \frac{1}{3} h^3 (1-h)^3 \mathcal{D}^{-1} H_2 \mathcal{F}^2 \, dx \leq 0, \end{aligned} \tag{D3}$$

where we have used (D1) to replace h_t , and the periodicity of h to remove the boundary terms when integrating by parts. The inequality in (D3) is proved on recalling that $\mathcal{D} > 0$ and $H_2 > 0$ from (2.8a) and (2.8c), respectively. The functional in (D2) can be written as

$$E(h) = -\frac{1}{2} C^{-1} B \|h\|_2^2 + \frac{1}{2} C^{-1} \|h_x\|_2^2 = \alpha_1 \|h\|_{H^1}^2 - \alpha_2 \|h\|_2^2, \tag{D4}$$

where $\alpha_1 = \frac{1}{2} C^{-1} > 0$ and $\alpha_2 = \frac{1}{2} C^{-1} (B + 1) > 0$. Here, $\|h\|_2$ denotes the L_2 -norm and $\|h\|_{H^1}^2 = \|h\|_2^2 + \|h_x\|_2^2$ is the norm defined in the H^1 Sobolev space comprising periodic functions in $[-L, L]$.

Using the interpolation inequality gives (e.g. Bertozzi & Pugh 1998)

$$\|h\|_2 \leq \gamma_1 \|h\|_{H^1}^{1/3} \|h\|_1^{2/3}, \tag{D5a}$$

where $\|h\|_1$ is the L_1 -norm and γ_1 is a positive constant. Applying Young's inequality to the right-hand side of (D5a) yields

$$\|h\|_2 \leq \gamma_1 \left(\frac{\varepsilon}{3} \|h\|_{H^1} + \frac{2}{3\sqrt{\varepsilon}} \|h\|_1 \right), \tag{D5b}$$

where ε is a positive constant, and hence

$$\|h\|_2^2 \leq \gamma_1^2 \left(\frac{\varepsilon^2}{9} \|h\|_{H^1}^2 + \frac{4}{9\varepsilon} \|h\|_1^2 + \frac{4\sqrt{\varepsilon}}{9} \|h\|_{H^1} \|h\|_1 \right) \leq 2\gamma_1^2 \left(\frac{\varepsilon^2}{9} \|h\|_{H^1}^2 + \frac{4}{9\varepsilon} \|h\|_1^2 \right). \tag{D5c}$$

By inserting the result in (D5c) into (D4), we establish that

$$E(h) \geq \tilde{\alpha}_1 \|h\|_{H^1}^2 - \tilde{\alpha}_2 \|h\|_1^2, \quad \text{or equivalently} \quad \|h\|_{H^1}^2 \leq \beta_1 E(h) + \beta_2 \|h\|_1^2. \tag{D6a,b}$$

Here, $\tilde{\alpha}_1 = \alpha_1 - 2\alpha_2\gamma_1^2\varepsilon^2/9$, $\tilde{\alpha}_2 = 8\alpha_2\gamma_1^2/(9\varepsilon)$ and $\beta_1 = 1/\tilde{\alpha}_1$, $\beta_2 = \tilde{\alpha}_2/\tilde{\alpha}_1$. We note that $\tilde{\alpha}_1$ is positive for small enough ε and $\tilde{\alpha}_2 > 0$ for any $\varepsilon > 0$, and hence we can ensure that both β_1, β_2 are positive by choosing ε to be sufficiently small.

Assuming a smooth initial condition $h(x, 0) = h^{(0)}(x) \in H^1$ satisfying periodicity in the domain $[-L, L]$, then the norm $\|h\|_{H^1}$ is uniformly bounded since from (D6) we find

$$\|h\|_{H^1}^2 \leq \beta_1 E(h^{(0)}) + \beta_2 \|h^{(0)}\|_1^2 \equiv \bar{C}, \tag{D7}$$

using the result in (D3) and conservation of volume, i.e. $\|h\|_1 = \|h^{(0)}\|_1$, which follows immediately from (D1). This proves that the Sobolev norm of the solution h is bounded for all $t > 0$.

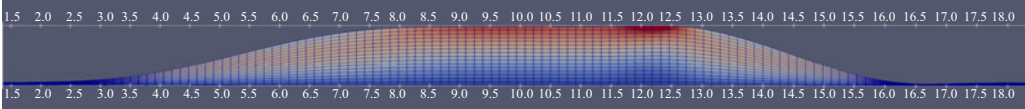


Figure 14. Lower fluid mesh from a DNS in oomph-lib, using 600 elements in the horizontal direction and 16 elements in the vertical direction in each fluid layer. The saturated interfacial profile shown is obtained for $B = 1$. The colour corresponds to the horizontal velocity in the lower fluid, varying from 0 (blue) on the lower channel wall to 1 (red) on the upper wall. The fluid is seen to move slightly faster than the upper wall (darker red colour) right before the capillary ridge at $x = 12.5$.

We use this boundedness result to show that the interface cannot touch the channel walls in finite time. We start by tracking the time evolution of the two spatial integrals

$$\frac{d}{dt} \int_{-L}^L \frac{1}{h} dx = \int_{-L}^L -\frac{h_t}{h^2} dx = \frac{2}{3} \int_{-L}^L h_x (1-h)^3 \mathcal{D}^{-1} H_2 \mathcal{F} dx \quad (\text{D8a})$$

and

$$\frac{d}{dt} \int_{-L}^L \frac{1}{(1-h)} dx = \int_{-L}^L \frac{h_t}{(1-h)^2} dx = \frac{2}{3} \int_{-L}^L h_x h^3 \mathcal{D}^{-1} H_2 \mathcal{F} dx, \quad (\text{D8b})$$

where in both integrals we have substituted the expression for h_t from (D1) and integrated by parts. The upper bound $\mathcal{D}^{-1} H_2 \leq \max\{1, m^{-1}\} \equiv \mathcal{M}$ is valid for $0 < h < 1$ (in fact, the bound of 1 or m^{-1} is approached when $h \approx 0$ or $h \approx 1$, respectively). Using this result and the definition of \mathcal{F} from (2.8d), we can show that the integrals on the far right-hand sides in (D8) are bounded by

$$\begin{aligned} \frac{2}{3} \mathcal{M} C^{-1} \int_{-L}^L h_x (B h_x + h_{xxx}) dx &= \frac{2}{3} \mathcal{M} C^{-1} \left(B \|h_x\|_2^2 - \|h_{xx}\|_2^2 \right) \\ &\leq a \|h_x\|_2^2 \leq a \|h_x\|_2^2 + a \|h\|_H^2 = a \|h\|_H^2 \leq a \bar{C}, \end{aligned} \quad (\text{D9})$$

with $a = \frac{2}{3} \mathcal{M} C^{-1} B > 0$. The last step in (D9) applies the uniform bound result shown earlier in (D7). We have therefore proved that the spatial integrals of h^{-1} and $(1-h)^{-1}$ remain bounded over a finite time interval. This result can be used to show that a solution satisfying $0 < h < 1$ initially, will satisfy this condition at all (finite) times; equivalently, that is to say the interface will not touch down/up in finite time. The rest of the proof is based on Agmon’s inequality (Agmon 1965) and can be completed in the same way as in Tseluiko & Papageorgiou (2007).

Appendix E. Details of the oomph-lib implementation

The governing equations are discretised in space using the finite-element method and in time using the second-order-accurate backward differentiation formulae (BDF). A Newton solver is then applied to solve the fully space–time discretised system, and adaptive time stepping is employed so that a temporal root-mean-square error norm (based on the difference between a prediction and the computed solution) remains below a tolerance of 10^{-5} . We refer the reader to the oomph-lib webpage (Heil & Hazel 2006b) for more details on the methods used.

The mesh is based on quadrilateral Crouzeix–Raviart elements and the method of spines is used to approximate the nodal position of the interface at a given location. A simulation for $B = 1$ uses 600 elements in the horizontal direction and 16 elements in the vertical

direction in each fluid layer. These parameters were found to be sufficient to produce accurate results, in the sense that simulations with double resolution gave interfacial profiles that are visually indistinguishable from those seen in figure 9. An example of the mesh for the highly deformed saturated state obtained for $B = 1$ is depicted in figure 14. We note that smaller values of B produce less deformed interfacial structures and hence require fewer elements to produce accurate results.

REFERENCES

- AGMON, S. 1965 *Lectures on Elliptic Boundary Value Problems*. AMS Chelsea Publishing.
- ANDERSON, T.G., CIMPEANU, R., PAPAGEORGIOU, D.T. & PETROPOULOS, P.G. 2017 Electric field stabilization of viscous liquid layers coating the underside of a surface. *Phys. Rev. Fluids* **2**, 054001.
- BABCHIN, A.I., FRENKEL, A.L., LEVICH, B.G. & SIVASHINSKY, G.I. 1983 Nonlinear saturation of Rayleigh–Taylor instability in thin films. *Phys. Fluids* **26** (11), 3159–3161.
- BARANNYK, L.L., PAPAGEORGIOU, D.T., PETROPOULOS, P.G. & VANDEN-BROECK, J.-M. 2015 Nonlinear dynamics and wall touch-up in unstably stratified multilayer flows in horizontal channels under the action of electric fields. *SIAM J. Appl. Maths* **75** (1), 92–113.
- BERTOZZI, A.L., MÜNCH, A. & SHEARER, M. 1999 Undercompressive shocks in thin film flows. *Physica D* **134** (4), 431–464.
- BERTOZZI, A.L. & PUGH, M.C. 1998 Long-wave instabilities and saturation in thin film equations. *Commun. Pure Appl. Maths* **51**, 625–661.
- BLYTH, M.G. & POZRIKIDIS, C. 2004 Effect of surfactants on the stability of two-layer channel flow. *J. Fluid Mech.* **505**, 59–86.
- BRETHERTON, F.P. 1961 The motion of long bubbles in tubes. *J. Fluid Mech.* **10** (2), 166–188.
- BURGESS, J.M., JUEL, A., MCCORMICK, W.D., SWIFT, J.B. & SWINNEY, H.L. 2001 Suppression of dripping from a ceiling. *Phys. Rev. Lett.* **86** (7), 1203–1206.
- CHAMPNEYS, A.R. & SANDSTEDE, B. 2007 Numerical computation of coherent structures. In *Numerical Continuation Methods for Dynamical Systems* (ed. B. Krauskopf, H.M. Osinga & J. Galán-Vioque), pp. 331–358. Springer.
- CHANDRASEKHAR, S. 1981 *Hydrodynamic and Hydromagnetic Stability*. Dover Publications.
- CHANG, H.-C., DEMEKHIN, E.A. & KAL Aidin, E. 2000 Coherent structures, self-similarity, and universal roll wave coarsening dynamics. *Phys. Fluids* **12** (9), 2268–2278.
- CHARRU, F. & FABRE, J. 1994 Long waves at the interface between two viscous fluids. *Phys. Fluids* **6** (3), 1223–1235.
- CIMPEANU, R., PAPAGEORGIOU, D.T. & PETROPOULOS, P.G. 2014 On the control and suppression of the Rayleigh–Taylor instability using electric fields. *Phys. Fluids* **26**, 022105.
- COLE, R.L. & TANKIN, R.S. 1973 Experimental study of Taylor instability. *Phys. Fluids* **16**, 1810–1815.
- DOEDAL, E.J. & OLDMAN, B.E. 2009 AUTO-07P: Continuation and bifurcation software for ordinary differential equations. Available at <http://cmvl.cs.concordia.ca/autol/>.
- ELGOWAINY, A. & ASHGRIZ, N. 1997 The Rayleigh–Taylor instability of viscous fluid layers. *Phys. Fluids* **9** (6), 1635–1649.
- EMMONS, H.W., CHANG, C.T. & WATSON, B.C. 1960 Taylor instability of finite surface waves. *J. Fluid Mech.* **7**, 177–193.
- FERMIGIER, M., LIMAT, L., WESFREID, J.E., BOUDINET, P. & QUILLIET, C. 1992 Two-dimensional patterns in Rayleigh–Taylor instability of a thin layer. *J. Fluid Mech.* **236**, 349–383.
- FRENKEL, A.L. & HALPERN, D. 2000 On saturation of Rayleigh–Taylor instability. In *IUTAM Symp. on Nonlinear Waves in Multiphase Flow* (ed. H. Chang), pp. 69–79. Kluwer.
- FRENKEL, A.L. & HALPERN, D. 2017 Surfactant and gravity dependent instability of two-layer Couette flows and its nonlinear saturation. *J. Fluid Mech.* **826**, 158–204.
- GLASNER, K.B. & WITELSKI, T.P. 2003 Coarsening dynamics of dewetting films. *Phys. Rev. E* **67**, 016302.
- HALPERN, D. & FRENKEL, A.L. 2001 Saturated Rayleigh–Taylor instability of an oscillating Couette film flow. *J. Fluid Mech.* **446**, 67–93.
- HAMMOND, P.S. 1983 Nonlinear adjustment of a thin annular film of viscous fluid surrounding a thread of another within a circular cylindrical pipe. *J. Fluid Mech.* **137**, 363–384.
- HEIL, M. & HAZEL, A.L. 2006a oomph-lib – an object-oriented multi-physics finite-element library. In *Fluid–Structure Interaction* (ed. M. Schäfer & H.-J. Bungartz). Springer.
- HEIL, M. & HAZEL, A.L. 2006b oomph-lib open-source software. <http://www.oomph-lib.org>.

- HOOPER, A.P. & GRIMSHAW, R. 1985 Nonlinear instability at the interface between two viscous fluids. *Phys. Fluids* **28** (1), 37–45.
- JENSEN, O.E. 2000 Draining collars and lenses in liquid-lined vertical tubes. *J. Colloid Interface Sci.* **221**, 38–49.
- KALOGIROU, A. 2018 Instability of two-layer film flows due to the interacting effects of surfactants, inertia and gravity. *Phys. Fluids* **30**, 030707.
- KALOGIROU, A. & BLYTH, M.G. 2020 Nonlinear dynamics of two-layer channel flow with soluble surfactant below or above the critical micelle concentration. *J. Fluid Mech.* **900**, A7.
- KALOGIROU, A., CIMPEANU, R. & BLYTH, M.G. 2020 Asymptotic modelling and direct numerical simulations of multilayer pressure-driven flows. *Eur. J. Mech. (B/Fluids)* **80**, 195–205.
- KALOGIROU, A., CIMPEANU, R., KEAVENY, E.E. & PAPAGEORGIOU, D.T. 2016 Capturing nonlinear dynamics of two-fluid Couette flows with asymptotic models. *J. Fluid Mech.* **806**, R1.
- KALOGIROU, A. & PAPAGEORGIOU, D.T. 2016 Nonlinear dynamics of surfactant-laden two-fluid Couette flows in the presence of inertia. *J. Fluid Mech.* **802**, 5–36.
- KAWAHARA, T. 1983 Formation of saturated solitons in a nonlinear dispersive system with instability and dissipation. *Phys. Rev. Lett.* **51** (5), 381–383.
- KAWAHARA, T. & TOH, S. 1988 Pulse interactions in an unstable dissipative-dispersive nonlinear system. *Phys. Fluids* **31** (8), 2103–2111.
- KITAVTSEV, G. 2014 Coarsening rates for the dynamics of slipping droplets. *Eur. J. Appl. Maths* **25**, 83–115.
- KOFMAN, N., ROHLFS, W., GALLAIRE, F., SCHEID, B. & RUYER-QUIL, C. 2018 Prediction of two-dimensional dripping onset of a liquid film under an inclined plane. *Intl J. Multiphase Flow* **104**, 286–293.
- KOPBOSYNOV, B.K. & PUKHNACHEV, V.V. 1986 Thermocapillary flow in thin liquid films. *Fluid Mech. Sov. Res.* **15** (1), 95–106.
- KULL, H.J. 1991 Theory of the Rayleigh–Taylor instability. *Phys. Rep.* **206** (5), 197–325.
- LANDAU, L.D. & LEVICH, B. 1942 Dragging of a liquid by a moving plate. *Acta Physicochim. URSS* **17**, 42–54.
- LEWIS, D.J. 1950 The instability of liquid surfaces when accelerated in a direction perpendicular to their planes. II. *Proc. R. Soc. Lond. A* **202**, 81–96.
- LISTER, J.R., RALLISON, J.M., KING, A.A., CUMMINGS, L.J. & JENSEN, O.E. 2006 Capillary drainage of an annular film: the dynamics of collars and lobes. *J. Fluid Mech.* **552**, 311–343.
- MAVROMOUSTAKI, A., MATAR, O.K. & CRASTER, R.V. 2010 Shock-wave solutions in two-layer channel flow. I. One-dimensional flows. *Phys. Fluids* **22**, 112102.
- MAVROMOUSTAKI, A., MATAR, O.K. & CRASTER, R.V. 2011 Shock-wave solutions in two-layer channel flow. II. Linear and nonlinear stability. *Phys. Fluids* **23**, 112101.
- NEWHOUSE, L.A. & POZRIKIDIS, C. 1990 The Rayleigh–Taylor instability of a viscous liquid layer resting on a plane wall. *J. Fluid Mech.* **217**, 615–638.
- OOMS, G., SEGAL, A. & CHEUNG, S.Y. 1985 Propagation of long waves of finite amplitude at the interface of two viscous fluids. *Intl J. Multiphase Flow* **11**, 481–502.
- ORON, A., DAVIS, S.H. & BANKOFF, S.G. 1997 Long-scale evolution of thin liquid films. *Rev. Mod. Phys.* **69** (3), 931–980.
- PAPAGEORGIOU, D.T., MALDARELLI, C. & RUMSCHITZKI, D.S. 1990 Nonlinear interfacial stability of core-annular film flows. *Phys. Fluids* **2** (3), 340–352.
- PAPAGEORGIOU, D.T., PETROPOULOS, P.G. & VANDEN-BROECK, J.-M. 2005 Gravity capillary waves in fluid layers under normal electric fields. *Phys. Rev. E* **72**, 051601.
- RAYLEIGH, LORD 1883 Investigation of the character of the equilibrium of an incompressible heavy fluid of variable density. *Proc. Lond. Math. Soc.* **14**, 170–177.
- RAZIS, D., EDWARDS, A.N., GRAY, J.M.N.T. & VAN DER WEELE, K. 2014 Arrested coarsening of granular roll waves. *Phys. Fluids* **26**, 123305.
- SANDSTEDTE, B. 2002 Stability of travelling waves. In *Handbook of Dynamical Systems* (ed. B. Fiedler), vol. 2, pp. 983–1055. Elsevier.
- SHARP, D. 1984 An overview of Rayleigh–Taylor instability. *Physica D* **12**, 3–18.
- TAYLOR, G. 1950 The instability of liquid surfaces when accelerated in a direction perpendicular to their planes. I. *Proc. R. Soc. Lond. A* **201**, 192–196.
- TAYLOR, G.I. & MCEWAN, A.D. 1965 The stability of a horizontal fluid interface in a vertical electric field. *J. Fluid Mech.* **22** (1), 349–383.
- TILLEY, B.S., DAVIS, S.H. & BANKOFF, S.G. 1994 Nonlinear long-wave stability of superposed fluids in an inclined channel. *J. Fluid Mech.* **277**, 55–83.
- TREFETHEN, L.N. 2000 *Spectral Methods in Matlab*. SIAM.

- TRINH, P.H., KIM, H., HAMMOUD, N., HOWELL, P.D., CHAPMAN, S.J. & STONE, H.A. 2014 Curvature suppresses the Rayleigh–Taylor instability. *Phys. Fluids* **26**, 051704.
- TSELUIKO, D. & PAPAGEORGIOU, D.T. 2007 Nonlinear dynamics of electrified thin liquid films. *SIAM J. Appl. Maths* **67** (5), 1310–1329.
- WANG, Q., MÄHLMANN, S. & PAPAGEORGIOU, D.T. 2009 Dynamics of liquid jets and threads under the action of radial electric fields: microthread formation and touchdown singularities. *Phys. Fluids* **21**, 032109.
- WANG, Q. & PAPAGEORGIOU, D.T. 2018 Using electric fields to induce patterning in leaky dielectric fluids in a rod-annular geometry. *IMA J. Appl. Maths* **83**, 24–52.
- WOLF, G.H. 1970 Dynamic stabilization of the interchange instability of a liquid–gas interface. *Phys. Rev. Lett.* **24** (9), 444.
- YIANTSIOS, S.G. & HIGGINS, B.G. 1989 Rayleigh–Taylor instability in thin viscous films. *Phys. Fluids A* **1** (9), 1484–1501.
- YIH, C.-H. 1967 Instability due to viscosity stratification. *J. Fluid Mech.* **27**, 337–352.
- ZHOU, G. & PROSPERETTI, A. 2022 Dripping instability of a two-dimensional liquid film under an inclined plate. *J. Fluid Mech.* **932**, A49.